FLAME FRONT ANALYSIS OF ETHANOL, BUTANOL, ISO-OCTANE AND GASOLINE IN A SPARK-IGNITION ENGINE USING LASER TOMOGRAPHY AND INTEGRAL LENGTH SCALE MEASUREMENTS

P.G. Aleiferis* and M.K. Behringer

Department of Mechanical Engineering, University College London, UK

*Author for Correspondence:

Prof. Pavlos Aleiferis

University College London

Department of Mechanical Engineering

Torrington Place, London WC1E 7JE, UK

E-mail: p.aleiferis@ucl.ac.uk

Currently:

Prof. Pavlos Aleiferis

Imperial College London

Department of Mechanical Engineering

Exhibition Road, London SW7 2AZ, UK

E-mail: p.aleiferis@imperial.ac.uk

Full length article accepted for publication by Combustion and Flame

ABSTRACT

Direct-injection spark-ignition engines have become popular due to their flexibility in injection strategies and higher efficiency; however, the high-pressure in-cylinder injection process can alter the airflow field by momentum exchange, with different effects for fuels of diverse properties. The current paper presents results from optical studies of stoichiometric combustion of ethanol, butanol, *iso*-octane and gasoline in a direct-injection spark-ignition engine run at 1500 RPM with 0.5 bar intake plenum pressure and early intake stroke fuel injection for homogeneous mixture preparation. The analysis initially involved particle image velocimetry measurements of the flow field at ignition timing with and without fuelling for comparison. Flame chemiluminescence imaging was used to characterise the global flame behaviour and double-pulsed Laser-sheet flame tomography by Mie scattering to quantify the local topology of the flame front. The flow measurements with fuel injection showed integral length scales of the same order to those of air only on the tumble plane, but larger regions with scales up to 9 mm on the horizontal plane. Averaged length scales over both measurement planes were between 4–6 mm, with ethanol exhibiting the largest and butanol the smallest. In non-dimensional form, the integral length scales were up to 20% of the clearance height and 5–12% of the cylinder bore. Flame tomography showed that at radii between 8–12 mm, ethanol was burning the fastest, followed by butanol, *iso*-octane and gasoline. The associated turbulent burning velocities were 4.6–6.5 times greater than the laminar burning velocities and about 13–20% lower than those obtained by flame chemiluminescence imaging. Flame roundness was 10–15% on the tomography plane, with largest values for ethanol, followed by butanol, gasoline and *iso*-octane; chemiluminescence imaging showed larger roundness (18–25%), albeit with the same order amongst fuels. The standard deviation of the displacement of the instantaneous flame contour from one filtered by its equivalent radius was obtained as a measure of flame brush thickness and correlated strongly with the equivalent flame radius; when normalised by the radius, it was 4–6% for all fuels. The number of crossing points between instantaneous and filtered flame contour showed a strong negative correlation with flame radius, independent of fuel type. The crossing point frequency was 0.5–1.6 mm^{-1}. The flame brush thickness was about $1/10^{th}$ of the integral length scale. A positive correlation was found between integral length scale and flame brush thickness and a negative correlation with crossing frequency.

INTRODUCTION

BACKGROUND

Combustion of Alcohols in Engines

Climate change and security of fuel supply both dictate diversification towards more sustainable bio-derived fuel stock. Ethanol is one of the preferred renewable additives to gasoline. Amongst its favourable properties is the high Research Octane Number (RON). Ethanol's high latent heat of evaporation can also be exploited in parallel to its high RON by enabling higher compression ratios for greater thermal efficiency. Gasoline already contains 5–10% ethanol in many countries (E5–E10) and can be compatible with existing fuel and combustion systems; however, its use will have limited impact on CO_2 emissions. Therefore, some markets are demanding much higher blending ratios, like E85, or even pure ethanol. However, such blends can lead to problems from excessive charge cooling and poor evaporation [1]. Butanol is a new alternative fuel with potential to play a strong role. Butanol's compatibility with common materials means that no major modifications are required to existing systems for fuel transportation and fuel injection in engines. Butanol is also less hygroscopic than ethanol with higher heating value. Fundamental understanding of the behaviour and effects of ethanol and butanol on in-cylinder combustion processes is an essential challenge in managing fuel flexibility and achieving lower CO_2 emissions. Several studies of ethanol combustion have been carried out in SI engines, focusing mainly on performance characteristics and exhaust emission measurements. However, most of these were done with Port Fuel Injection (PFI) systems [2–11]. Butanol has been studied in the literature much less than ethanol, *e.g*. see [12–17]. Very few alcohol studies have been conducted in latest technology Direct Injection Spark-Ignition (DISI) engines that are typically very sensitive to fuel properties. More to the point, many of those studies illustrate diverse effects over different mixture preparation methods and regimes of operation [18–23].

Burning Velocities of Alcohols and Hydrocarbons

A major aspect of understanding combustion of fuels in engines is their laminar and turbulent burning velocities in controlled environments and at engine-relevant conditions. Laminar burning velocities have been measured for a range of hydrocarbon and alcohol fuels at various conditions by [24–27] among others. More recently, results have been reported by [28–29] for ethanol, [30] for *iso*-octane, [31] for primary reference fuels and gasoline, [32–33] for butanol and by [34–36] for most of these fuels. A large database of fuel structure effects has also been produced by [37]. These authors reported data derived from thermodynamic analysis of pressure traces from explosions in a combustion vessel, typically at 3 bar and 450 K, following the approach of [26]. However, the velocities obtained were larger than those of other existing data for alkanes and aromatics by as much as 30%. The authors commented that this was due to different measurement techniques, *i.e.* thermodynamic (heat release) *vs.* optical (entrainment). This highlights issues that can lead to differences among authors, *e.g.* flame cellularity effects at high pressure, the specifics of various methodologies used to derive unstretched values of burning velocity, *etc.* Furthermore, in most of the published databases, the effect of burned gas on laminar burning velocity has not been quantified in detail and hence very few data exist that are directly relevant to realistic in-cylinder conditions. The overall effect of burned gas residuals on burning velocities has been quantified to be much stronger than that of excess air, temperature or pressure; with residual fractions of 0.15–0.2, the laminar burning velocity of *iso*-octane has

been found to decrease by 35–45% according to Metghalchi and Keck [26]. Such levels of residuals are commonly found in DISI engines at part-load operation or when Exhaust Gas Recirculation (EGR) systems are employed to control NO_x formation over a range of loads. Marshall *et al.* [38] published recently measured laminar burning velocities at engine-like conditions with and without residuals for various liquid fuels, including *iso*-octane and ethanol and discussed several effects in comparison to the data of [26]. Vancoillie *et al.* [39] also presented a review of laminar burning velocities and new correlations for the operating range of alcohol-fuelled SI engines. The recent studies of Broustail *et al.* [40, 41] on the laminar burning characteristics of ethanol/*iso*-octane and butanol/*iso*-octane blends at engine-relevant conditions are also noteworthy. In contrast, limited data exist on turbulent burning velocities at engine-relevant conditions for liquid fuels [42–44]. Bradley and co-workers [45–46] have published turbulent burning velocities for *iso*-octane, methanol and ethanol, but no complete data sets really exist with presence of residuals and for longer chain alcohols. Furthermore, despite efforts that have quantified turbulent flame speeds in DISI engines by direct flame visualisation (chemiluminescence) with a variety of fuels, including *iso*-octane, gasoline, ethanol, butanol and some of their blends [47–51], very little information exists on flame speeds obtained by planar imaging techniques in modern geometry SI engines, *e.g.* see [52, 53], but no detailed planar data have been derived specifically with ethanol and butanol fuels in direct comparison to *iso*-octane and gasoline.

PRESENT CONTRIBUTION

When one considers the need for fundamental understanding of in-cylinder combustion processes with diverse fuels it is surprising that no major studies have compared in detail the in-cylinder behaviour of typical liquid hydrocarbon fuels to that of ethanol and butanol in latest geometry DISI engines. Recently Aleiferis and co-workers [50, 51] published combustion data of heat release, in-cylinder flame expansion speeds and flame centroid motion obtained by crank-angle resolve flame chemiluminescence imaging of *iso*-octane, gasoline, ethanol and butanol fuels in comparison to gaseous methane fuelling by port fuel injection. The present study aimed at going a step further by quantifying and discussing in-cylinder flame front topologies of ethanol, butanol, *iso*-octane and gasoline fuels obtained by planar Laser-sheet flame visualisation. The main objective was to quantify the degree of flame front distortion and wrinkling for these fuels with respect to in-cylinder flow and integral length scales. Therefore, the analysis also involved characterisation of the in-cylinder flow field and quantification of the integral length scales of turbulence at ignition timing by Particle Image Velocimetry (PIV). Laser Doppler Velocimetry (LDV) data from the same engine [54, 55] were also consulted to assist the discussion. To the best of the authors' knowledge, this is the first time that such a set of complete data is presented for these fuels in a latest geometry SI combustion system. The presented measurements contribute towards a database of in-cylinder turbulent flame behaviour and combustion rates which are essential for developing our fundamental understanding of the underlying phenomena at realistic engine conditions. Such data can also be useful to combustion modellers because simulation and validation of in-cylinder flame growth phenomena with various fuels is still very challenging.

EXPERIMENTAL APPARATUS AND PROCEDURES

FUELS

Four fuels were investigated: a typical commercial grade gasoline (RON95) without oxygenates, *iso*-octane, ethanol and *n*-butanol (1-butanol). A standard gasoline blend contains several hundred hydrocarbons,

typically about 25%–30% C_5 or lower, 30%–40% C_6–C_8 and the remainder C_9–C_{10} hydrocarbons. *Iso*-octane is one of the major single components of gasoline, with a boiling point of 99 °C at atmospheric pressure; *n*-butanol boils at 117 °C whilst ethanol boils at 78.4 °C. **Table 1** provides a quick overview of various thermophysical properties of these fuels; the distillation curve of the specific gasoline used has been shown elsewhere [56, 57]. Summarising published data, Aleiferis *et al.* [51] tabulated laminar burning velocities at ϕ=1.0 and ϕ=0.5 for these fuels at pressure and temperature conditions relevant to those expected at the start of combustion in SI engines. **Tables 2** displays mean values from that exercise for immediate reference where it is apparent that differences amongst fuels at high pressure are quite small. Although experimental uncertainties of the order 1 cm/s typically exist, there is a decrease in burning velocity with decreasing pressure, increasing temperature and departure from stoichiometry on the lean side, as well as with increasing carbon chain length for the alcohols.

RESEARCH ENGINE

A single-cylinder optical research engine was used for the present work. This has been designed and built by MAHLE Powertrain UK with its optical geometric design features optimised over several years of research at UCL. Details about the engine and the test bed arrangement can be found in previous publications by the current authors, *e.g.* [13, 20, 54], hence only the most relevant features are described in this section. Important engine parameters are summarised in **Table 3**.

The research engine head was based on a serial production 4-cylinder 2-litre 16-valve engine. A single-hole swirl-type DI injector was mounted on the side of the combustion chamber between the intake valves. The fuel was supplied to the injector by a Heypac GX30 pneumatic pump and regulator; the injection pressure was fixed at 80 bar throughout the current study. The crank and cam shafts were equipped with shaft encoders resolving 1800 increments per revolution. An AVL427 engine timing unit was employed for ignition and injection control, as well as for provision of synchronised triggering to Lasers and cameras. The spark was generated by a triple platinum electrode spark plug powered by a coil-on-plug ignition system. A typical Bowditch piston arrangement with a 45° mirror allowed visual access to the combustion chamber. The top of the Bowditch carried a titanium piston crown holding a circular sapphire window. Piston rings made from Torlon were used and operated unlubricated. A full-stroke optical liner made entirely from fused silica was used for optical experiments not requiring ignition and a semi-optical liner allowing side access to the combustion chamber was used for horizontal Laser flame tomography during engine firing. The latter arrangement employed a flat pentroof window of 9 mm thickness and 43 mm width.

MEASUREMENT TECHNIQUES

Testing Arrangements and Data Acquisition

Acquisition of pressure and temperature data was realised by a 12-bit National Instruments (NI) PCI-6023E DAQ card capable of a sampling rate of 200 kS/s for 16 channels. Pressure sensors with respective amplifiers for in-cylinder pressure, intake plenum pressure, intake runner and exhaust pressure were used, logged and referenced as needed (Kistler 6041A, 4075A10V39, Kistler 4045A2V39, Kistler 7531, respectively). Their digitisation rate corresponded to 0.2° CA at 1500 RPM. The uncertainty due to electrical interference was a maximum of 0.05% of the full-scale value for the in-cylinder pressure and 1% of the full-scale value for the intake plenum and other pressures, corresponding to a typical uncertainty of ±5.0 mbar and ±10 mbar,

respectively. Pressure data were post-processed to calculate the Indicated Mean Effective Pressure (IMEP), amplitude and timing of peak in-cylinder pressure, including mean values and Coefficients of Variation (COV=Mean/RMS). Heat release analysis and calculation of Mass Fraction Burned (MFB) was performed using methods based on [58, 59] and followed practices of earlier work by the current authors for consistency [13, 20, 21, 48–51]. All uncertainties involved in acquiring and processing in-cylinder pressure data were carefully considered according to [60]. A representative number of cycles for statistical analysis was identified on the basis of COV_{IMEP}. This achieved steady-state values at about 150–200 cycles, hence 200 cycles were typically used for each test point analysis, unless otherwise stated.

All experiments were conducted at an engine speed of 1500 RPM with 0.5 bar intake plenum pressure. This condition represents a typical fuel saving operating point during driving. Engine head and metal liner temperatures were kept at 80 °C to represent warm engine-running conditions. The ignition timing was fixed to gasoline's minimum spark advance for best torque (MBT) obtained during engine mapping experiments. This was 26 °CA BTDC (=Crank Angle Before firing Top Dead Centre) for stoichiometric fuelling. It is also noted that the IMEP *vs.* spark advance curve was fairly flat around this ignition timing for all fuels. The injection timing was fixed to 60 °CA ATDC (after intake TDC) for homogeneous mixture preparation; this was based on earlier work with various injection timings and fuels that had optimised injection timing in order to allow maximum time available for evaporation up to ignition timing but also minimise piston-crown spray impingement during injection. The injection duration was adjusted with each fuel for stoichiometric Air-to-Fuel Ratio (AFR) conditions according to a wide-range lambda sensor and AFR1200 recorder. In that respect, the injection pulse length for gasoline and *iso*-octane was 1.26 ms. In contrast, for butanol this was 1.50 ms and for ethanol much larger at 1.85 ms. All timings given in °CA refer to the 'crank angle time equivalent' at 1500 RPM, with one 1 °CA corresponding to 0.111 ms.

Flow Characterisation

For PIV and tomography measurements, oil droplets with a density of 920 kg/m^3 were created by an atomisation seeder and introduced into the engine's intake flow on four evenly distributed ports around the intake runner approximately 150 mm upstream the intake valves. The seeding particles were measured regarding their size in free flow at atmospheric conditions and were found to be about 1–2 μm in diameter. Studying particle-size histograms and considering size changes at lower initial pressures and with increasing temperatures, calculation of particle response times showed that the seeding would respond well to flow frequencies of the order 0.1 °CA. To bring this into context, the integral timescale in this engine measured by LDV at ignition timing was of the order 8–16 °CA (depending on velocity component) [54, 55].

The PIV experiments were specifically performed to quantify the effect of fuelling in the intake stroke on the in-cylinder air flow structures and integral length scales in the vicinity of the spark plug late in the compression stroke at ignition timing. The Laser/camera arrangement was based on a Quantel Big Sky ULTRA CFR 120 Nd:YAG Laser (120 mJ per pulse) and a TSI Powerview Plus 4 MP camera (2048×2048 pixels). Two in-cylinder planes were considered, a horizontal plane (also called 'swirl' plane hereafter) located 1 mm below the spark plug's ground electrode (or 3 mm above the fire-face) and another one, vertical centrally located, cutting through the spark-plug from inlet to exhaust side (also called 'tumble' plane hereafter). Following extensive analysis on the minimum number of cycles required for representative

mean and turbulent fluctuations data from PIV data [54], a minimum of 540 individual cycles were averaged for each experimental test point in batches of 60 cycles per run; this practice of batching was based on the data storage capabilities of the imaging system and image quality deterioration by fowling of the optical access with increased duration of test runs. **Table 4** summarises the system's main settings. Several aspects of the PIV technique, including practical application and uncertainties (seeding particles per interrogation window, potential peak locking bias, *etc.*) were optimised according to Raffel *et al.* [61].

For the swirl view measurements, the Laser beam was converted to a sheet of ~0.5 mm thickness by a combination of spherical and cylindrical lenses, fired horizontally through the pent-roof of the engine in full optical setup (quartz liner and sapphire piston window); the camera was positioned in front of the 45° mirror that was situated within the Bowditch piston arrangement. The arrangement was reversed for the tumble plane measurements with the Laser firing at the 45° mirror and the camera aligned for pent-roof view access with the fully optical liner. After extensive testing, the Laser pulse separation was typically set at 10 μs; more details on the effect of pulse separation are discussed in the results section. The image resolution was 18.4 μm per pixel on the tumble plane and 34.6 μm per pixel on the swirl plane view. For completeness, it needs to be noted here that in fuelled-cycle experiments, both seeding particles and any remaining fuel spray droplets at ignition timing will contribute to measured velocities; this contribution ought to be made strictly without any bias between the two. Droplet sizing of the spray at the operating conditions of the engine was performed with all fuels [62] and it was found that any remaining droplets at ignition timing were very few and of similar size to the nominal size of the seeding particles.

Prior to calculating the velocity field, background removal was applied. Spurious velocity vectors were typically less than 1% and very few cycles with more spurious vectors than that, usually due to increased window fowling with ongoing measurement duration, were examined and exempted from the data set where necessary. Apart from ensemble-average flow fields, the turbulence intensity u', v', w' was also obtained as the RMS of the velocity measurements at each point. LDV measurements in the same engine [54] indicated that the air-flow during late compression was quite close to isotropy. Therefore, it was decided that the Turbulent Kinetic Energy (TKE) would be approximated by using the RMS of each velocity component at each point on that plane and estimating the 3rd velocity component as the arithmetic average of the other two; this approach is addressed further in the results section.

Cross-correlation coefficients were calculated at each point on the PIV flow fields and integral length scale maps were produced for all cases with and without fuelling for all velocity components (L_u, L_v, L_w). The integral length scale L_u is defined as the integral of the spatial correlation coefficient R_x of the fluctuation velocity u (*i.e.* instantaneous minus mean) at two adjacent points in space, one at x_0 and another one at a distance χ from x_0 as follows:

$$L_u = \int_0^\infty R_x dx\,, \qquad R_x = \frac{\overline{u(x_0,t)u(x_0+\chi,t)}}{u'(x_0,t)u'(x_0+\chi,t)}$$

where overbars denote spatial averaging (similarly for L_v and L_w). The integral timescales were also calculated using the autocorrelation coefficient (by time averaging) and available crank-angle resolved LDV airflow data from the same engine at the same conditions for further interpretation [55]. It is noted here that the PIV measurements campaign in this engine was much larger and what implied from the data set used in

the current paper; several parameters were studied, *e.g.* effect of engine head temperature, effect of injection duration (fixed and varying for all fuels), *etc.* This extended campaign and analysis solidified confidence to the conclusions of the subset of PIV data used in the current study. The complete set of data can be useful to the interested reader for broader interpretation of in-cylinder flow phenomena [54, 55, 62].

Flame Chemiluminescence Imaging and Processing

The flame radius can reveal details very early in the combustion process (0–5% MFB), a period that is not typically resolved well by thermodynamically derived MFB data. A high-speed camera Photron APX-RS was employed for this study. The camera was operated at 9,000 Hz, *i.e.* capturing one flame image per crank-angle degree at 1500 RPM. Details of the system have been described in previous studies and not repeated here for brevity [13, 20, 21, 47–51]. The fast shutter speed reduced background noise but also led to low combustion luminosity levels requiring small thresholding values for processing. A circular mask with a diameter slightly smaller than the piston window was laid over the original image to remove reflections from the metal housing of the optical crown. Then the image was binarised by thresholding and the flame outlining was obtained. **Figure 1** shows a typical flame chemiluminescence image with a superimposed flame outline as automatically identified. The flame size was measured and the equivalent flame radius, representing the radius of a circle with an area identical to that of the measured flame area A, was calculated as $r=(A/\pi)^{1/2}$. This practice provided data that could also be used for comparison with combustion vessel experiments where similar methods of quantification have been employed for laminar and turbulent flame speeds, *e.g.* from schlieren [27, 29, 42–46], as well as with previous studies in other SI engines of similar capacity and pentroof geometry, *e.g.* [51]. Even though simple, this method is believed to return very similar results to more complex elliptical fittings, except for the very early flame kernels, *e.g.* see [63]. In an attempt to quantify the flame front general distortion, the flame roundness was calculated as the degree by which the ratio of area to perimeter converged towards the circular shape following the relation $4\pi A/P^2$, where A the area and P the perimeter of the flame. This parameter is essentially the same ratio to that used recently by [52] for their in-cylinder flame tomography work of *iso*-octane, methane and propane fuels. However, one can derive various types of 'roundness' or 'wrinkling' parameters for a flame, with many different definitions used historically (ratio of instantaneous contour and filtered contour perimeter, ratio of instantaneous contour perimeter and circumference of circle of same area, *etc.* [64]); future work could focus on assessing several of those and discussing resultant trends with different fuels.

It is also noted for completeness that the chemiluminescence imaging campaign in this engine was much broader than the subset of data employed in this paper. Various effects were studied, *e.g.* effect of engine head temperature, effect of fuel blending, effect of equivalence ratio ϕ, effect of fuel type on flame intensity and colour, *etc.* To avoid deviation away from the specific objectives of the current study, this complete set of data is discussed in detail elsewhere for the interested reader [65]. Uncertainties in the processing methodology and calculated ensemble averaged flame areas were carefully estimated by considering binarised flames throughout the whole campaign. The area calculated for a flame image was compared to the measured area of the same flame image with an extra pixel added to the equivalent flame radius. This was considered to represent an uncertainty linked to the spatial resolution of the imaging arrangement; secondly, the change in the binarised area of a flame due a change in the threshold value was also computed. For very

small flames at ~10° CA after ignition (about 1–2 mm in radius depending on fuel, with 0% MFB calculated by heat release analysis of the respective pressure records) these uncertainties were found to be about 0.2–0.5% and 8–10% per threshold unit of the nominal equivalent flame radius, respectively. For larger flames at about 30° CA after ignition timing (corresponding typically to about 5–10% MFB depending on fuel), when considering a wider window of uncertainty of 10 pixels, the uncertainties were still quite low, about 0.5–2% and 1–2% of the equivalent flame radius, respectively. It is noted that the same order of uncertainties was quantified from a similar set of chemiluminescence measurements obtained from a different optical engine with a different injection system [51]; this fortified confidence to the conclusions presented later in terms of their engine-independent nature in broader terms.

Flame Tomography Imaging and Processing

The flame tomography experiment was conducted to obtain planar details of the flame front on the horizontal swirl plane that could not be identified by chemiluminescence imaging due to the projected line-of-sight nature of the latter technique. The basic setup was similar to that described in the PIV section with the intake air seeded in the same manner. The use of a PIV system as basis for this measurement allowed two successive images to be acquired within a short interval. As for the air-flow study, the flow field could be determined for locations with seed presence and the flame outlining could be obtained with suitable Laser pulse separation. For swirl plane imaging, the Laser entered the combustion chamber through the pent-roof window of the metal liner. The system was optimised for this application with the lens set to f/5.6 and the camera positioned as close as possible to the mirror to achieve a maximum resolution of 33.4 μm per pixel. A band-pass filter centred on the Laser's wavelength ±10 nm was placed in front of the camera lens to filter out any flame chemiluminescence light. The images were taken at various times after AIT to ensure that the flame was within the area illuminated by the Laser sheet. **Figure 2** shows a typical image of flame tomography with superimposed outlines of both flame exposures (the image's brightness has been boosted to enable better visual clarity for reproduction purposes).

It was found that at a timing of 15 °CA AIT, the flames of ethanol and butanol were already reasonably large but generally within the boundary limits of illumination. *Iso*-octane was, however, slower and adjustments were necessary. Within the objectives of the current study, it was finally decided to fix ignition timing for all fuels to gasoline's MBT of 26 °CA BTDC to enable nominally similar in-cylinder pressure and temperature conditions at the timing of spark for all tests. Then image acquisition timing was adjusted for each fuel to allow flames of similar mean size to be examined (9–10 mm in radius). Specifically, image acquisition was fixed at 15 °CA AIT for both ethanol and butanol fuels; this was delayed for gasoline by 1 °CA (16 °CA AIT), whilst *iso*-octane required an even larger delay of 3 °CA (18 °CA AIT). The effect of such differences in image acquisition time on the in-cylinder thermodynamic conditions was moderate due to the piston's proximity to TDC (3 °CA crank shaft rotation translated to ~0.5 mm vertical piston movement), such that the in-cylinder pressures at the imaging time frame were measured between 7.8–8.2 bar. Overall, 240 image pairs (frames A and B) were taken for each fuel, consisting of batches of 60 images; Laser pulse separations of 10, 25, 50 and 100 μs were tested. The pulse separation had to be limited within 10–25 μs for calculations of the local flame front speeds, as little benefit was gained for larger pulse separations where global flame convection became more obvious when calculating the displacement of the flame's geometric centroid.

Calculations of the equivalent flame expansion speed, however, profited from larger pulse separations. This will be discussed in more detail in the results section.

Local geometrical features of the flame front could be extracted from the frames returned by the planar Laser imaging system. For the flame's global expansion speed, both image frames had to be analysed; this speed was calculated as the flame radius growth rate of the equivalent areas between the two image frames in similar manner to the method used with the chemiluminescence images. The local distance between the flame front location on the two frames was extracted to obtain a localised flame speed. Another target was to obtain information about the unburned charge velocity in the immediate vicinity of the flame front by PIV, in an attempt to calculate the flame's turbulent burning velocity from the flame's expansion speed and the unburned charge velocity.

The image processing method consisted of a series of automated and manual inspection steps. Firstly background subtraction was applied. Approximately 20% of the images were not usable in the end, due to flame clipping by either the piston window or growth beyond the Laser sheet's width; also flames which appeared split into several unconnected sections were excluded from processing. To equalise image intensities of frames A and B (originating from small intensity differences per pulse between the two Laser cavities), an imaged region without flame was selected on one of the two frames and the other frame was amplified to match the first frame's intensity in this region. Furthermore, to enable continuous tracing, pixelation was removed by filtering, followed by binary conversion using Otsu's method (*e.g.* see [53, 64, 66]). Any residual noise caused by the spark plug ground electrode and the edges of the exhaust valves was finally manually removed. Finally, the flame's outline was traced. With the data obtained, it was possible to calculate the flame area, equivalent flame radius, roundness and centroid position similarly to the flame chemiluminescence imaging analysis; the probability of flame presence was also calculated.

An expanding flame 'sees' increasing number of sizes and frequencies of turbulent length scales as it grows, *i.e.* there is an 'effective' turbulence intensity associated with flame growth [67, 68]. Those scales that are larger than the size of the kernel will primarily 'convect' it without distortion (*e.g.* away from the spark-plug electrodes), whilst those smaller than the kernel will distort and/or wrinkle it depending on the degree of turbulence. Considering the challenges discussed in [42] with regards to deriving turbulent burning velocities even in homogeneous isotropic turbulence (where various radii definitions need to be considered for the quantification of burning rates and other quantities, e.g. crossing of the flame shape with the relevant spherical shape), a filtering methodology was adopted here for processing the flame tomography contours. Specifically, for information about the flame front distortion and wrinkling, a 'mean' flame contour was obtained with the actual flame fluctuating around it, as shown in **Figure 3**. To do that, the 2D flame outlining was converted into a complex function of the form $f(l) = y(l) + iz(l)$, with y and z representing the contour coordinates of the flame boundary and l being the curvilinear coordinate along the contour's length. A first-order low-pass filter was applied on the instantaneous contour with a cut-off frequency based on the equivalent flame radius to obtain a 'mean' flame contour. In order to obtain a 1D developed view from the 2D flame front in the images, the distance from the flame's geometrical centroid to the flame outlining was calculated and plotted against the curvilinear coordinate moving along the outlining. The distance from the geometrical flame centroid could be derived for each location of the instantaneous and filtered flame contour**.**

A plot of the instantaneous and filtered flame contours is shown against the curvilinear coordinate in green and blue respectively. Subtracting the filtered contour from the instantaneous contour returned the fluctuation around this filtered mean (red line).

The local flame speed at the flame front could be obtained at distinct locations on the flame border. The extraction of the local velocities at crests and cusps proofed to be the most difficult step in terms of processing. The main difficulties arose from the sensitivity to thresholding for very small pulse separations of 10 μs, while larger pulse separations were negatively affected by global convection and large distortion of the flame front. The global convection was partly accounted for by translatory adjustments of the second image's contour to match the area centroid of both image frames. The processing of the crest regions, which were distinguished by the raw flame contour being outside the filtered contour in both image frames, required the creation of the contour-normal for each measurement point of image frame A and the location of its intersection with the contour of image frame B. The local velocity was then obtained as the ratio of the distance between the intersection points to the pulse separation time. A three-point smoothing interval was used on the raw flame outlines to avoid excessive variations in the normal vectors. Finally, all images were visually validated and cycles with obvious errors were excluded. Examples of excluded images were due to strong differences from frame A to B caused by additional flame kernels or flame fingers appearing in the second frame, strong convection and contour thresholding difficulties. This reduced the number of usable cycles to about 150 out of 240, with more images discarded for the hydrocarbon than the alcohol fuels. Due to the resolution of the images and the low pixel displacement, a statistical analysis had to be performed especially for small pulse separations to resolve differences between fuels on a sub-pixel scale. For this, individual local velocities within an image were averaged. Calculations based on average flame speeds of 7 m/s, normally distributed with a standard deviation of 2 m/s (as typically shown during measurements), for a minimum of 1000 data points confirm to resolve differences of 0.5, 0.2, 0.1 and 0.05 m/s for pulse separations of 10, 25, 50 and 100 μs, respectively.

RESULTS AND DISCUSSION

FLOW MEASUREMENTS

Flow Field at Ignition Timing

Figure 4 shows the ensemble-averaged velocity and TKE fields of air only motoring measurements (*i.e.* without having injected any fuel in the intake stroke) for both vertical and horizontal planes. For positional clarity, these fields have been superimposed on a background image of the combustion chamber showing the spark plug protruding into the pentroof at the centre of the tumble plane view and the outlining of the valve edges and spark plug on the swirl plane view. The zero value on the x-axis of the tumble view shows the location of the engine's fire-face (TDC) with the piston top land being approximately 6 mm lower than that at the time of measurement. The swirl plane corresponds to x=3 mm on the tumble plane. Maximum velocities of about 5 m/s were present on the intake side just below the valve area (top left corner of the field), where the clockwise bulk tumble flow came into the image frame from the engine's squish area. The flow was successively forced against and around the spark plug. In the wake of the spark plug, velocities were strongly reduced to levels of 1–2 m/s, still predominantly in the direction of the exhaust port, with a recirculation zone towards the top right edge of the spark plug. Similar velocities were quantified on the

swirl plane, consistent with the tumble-view flow structures; high velocities were recorded on the intake side and low velocities past the spark plug on the exhaust side. The mean flow also showed two-counter rotating vortices with their centres located below each one of the intake valves. The TKE on the tumble plane was typically between 10–16 m^2/s^2 and featured increased levels in the area below the spark plug electrodes and towards the exhaust side. Similar values of TKE were obtained on the swirl plane, with largest values in the negative z-direction. When looking along the y-axis at z=0 where the tumble plane corresponded to, TKE values of up to about 13 m^2/s^2 were quantified. These lower values than the levels obtained on the tumble view at x=3 mm are essentially a result of the estimation of the 3rd velocity fluctuation component which was taken as the average of the two measured RMS components. Close statistical analysis of these PIV data, as well as of LDV data [54, 55], showed that w' was slightly lower than the mean of u' and v' (4–5%) which effectively translated to an overestimation of the TKE by ~20% on the PIV tumble plane when using the average of u' and v' as an estimation for w'. This should be borne in mind when making comparisons of data in the area of intersection between the two planes hereafter to avoid confusion.

The effects of the fuel injection process early in the intake stroke on the measured flow fields at ignition timing in the late compressions stroke are shown in **Figure 5**. These maps correspond to stoichiometric *iso*-octane fuelling. It is clear that fuelled cycles exhibited higher mean velocities in the intake region of the combustion chamber just under the valves. Specifically, the region with velocities of 5–6 m/s was much larger than that in the non-fuelled case of **Figure 4;** this was quite consistent with all fuels. Highest velocities were found in that region with stoichiometric gasoline fuelling, where the velocity region close to the intake valves showed magnitudes of 6 m/s that filled most of the area left of the spark plug. This was also associated with higher levels of TKE in the lower left region of the image. All fuels exhibited an increase in TKE in that region in comparison to the non-fuelled case, with stoichiometric gasoline and butanol fuelling showing values up to ~18 m^2/s^2, *i.e.* about 20% higher than the non-fuelled case. This behaviour was accompanied by a decrease in TKE on the right hand side of the image under the exhaust valves. Similar effects were also present on the swirl plane flow fields but the differences between fuelled and non-fuelled experiments appeared less pronounced. Generally, higher flow velocities along the y-axis seemed to correlate with smaller swirl-vortex diameters and closer swirl-vortex centres. Butanol exhibited the smallest difference between non-fuelled and fuelled case. In general the overall effect for all fuels can be summarised as a strengthening of the bulk motion, especially on the tumble plane. This can be attributed to the mechanism of momentum exchange between fuel spray and air motion during the earlier phases of the cycle. Decoupling the observed differences among fuels is not trivial and cannot be elaborated on within the bounds of the current publication. Therefore, extended discussion will form part of a separate dedicated publication on the basis of [61] where flow field changes with fuelling were studied over a range of conditions and linked by a combination of factors, such as the duration of injection, the droplet velocities and droplet sizes during injection, the fuel spray's shape during injection (*e.g.* see [19] for spray 'collapse' effects in this engine), *etc.* It is noted here, however, that experimentation with identical injection duration for all fuels led to smaller differences among recorded flow fields for all fuels and to smaller differences from the non-fuelled air only PIV experiments as well.

Integral Length Scales of Turbulence at Ignition Timing

Integral length scale maps for air only motoring experiments are provided in **Figure 6**. The length scale L_u in the x-direction obtained from the u-velocity data on the tumble plane had typically values between 2–5 mm, with largest scales towards the intake side and smallest scales primarily below the spark plug electrode. These values corresponded to about 20–25% of the maximum distance from piston top to engine head. This is broadly in agreement with integral length scales of about 15–20% the clearance height typically quoted in the literature from LDV measurements obtained as early as the mid-1980s in pancake combustion chambers [69]. The L_v scales along the y-axis for the swirl and tumble view measurements matched reasonably well, both showing increased values in comparison to L_u. Typically, the length scale obtained was about 10% larger for the swirl view than the tumble view, with length scales L_v between 5–8 mm along the y direction and values up to 8 mm on the side of the engine's positive z-axis. Therefore, the integral length scale was about 10% of the cylinder's bore diameter, except in the region of the tumble view where the spark plug was protruding into the cylinder disturbing the flow and leading to integral length scales of ~2 mm. The integral length scale L_w obtained from the velocity component in the z-direction on the swirl plane was generally lower than L_v with values between 3–7 mm.

The integral length scale maps obtained at ignition timing, after fuel injection had occurred in the intake stroke, are presented in **Figure 7** and **Figure 8** for the tumble and swirl planes, respectively. For the integral length scale of the vertical velocity component u, *i.e.* L_u, small differences were observed between fuels and with the air-only motoring case; maximum values of the order 5.5 mm were quantified on the left of the spark plug under the engine's intake valves in **Figure 7**. On the exhaust side, the scales dropped to levels of 2–4 mm. The horizontal length scale L_v (v-velocity component) showed larger differences between fuels and when compared to air-only experiments. Throughout all measurements, the maximum length scales were of the order of 8–9 mm, largest between piston top land and spark plug ground electrode. This is due to the physical boundary set by the spark plug and the pent-roof design which abruptly reduced the relevant scale to less than half the cylinder's diameter in the upper part of the combustion chamber. L_v generally increased, particularly for ethanol, and this was clear on both tumble and swirl views. In contrast, butanol showed the smallest difference in comparison to the non-fuelled air-flow case. In general, the w-component length scale, L_w, also exhibited an increase with most fuels when compared to the non-fuelled experiments; butanol posed an exception as the L_w map indicated generally smaller scales, particularly on the swirl plane. When averaging the length scale maps to obtain a single value for each component and then averaging both components on each plane, a mean length scale value L_{uv} was obtained from the tumble plane experiments and a respective L_{vw} from the swirl plane, as summarised in **Table 5**. Resulting values of L_{uv} were between 3.9 mm to 4.6 mm, with ethanol having the largest and butanol the lowest integral length scales. L_{vw} values were between 4.9 mm to 5.7 mm, with ethanol again largest and butanol smallest.

FLAME MEASUREMENTS

Flame Chemiluminescence Area and Radius Growth

To set initially the scene of combustion differences between the single component fuels in this engine, **Figure 9** shows the percentage of the piston crown window area occupied by the flame during its growth and the equivalent flame radius growth; the curves are averages of the multi-cycle crank-angle resolved

chemiluminescence imaging data. 100% signifies that the enflamed area, as recorded by the camera, covered the whole of the optical crown's circular area; it is also noted that 100% of the optical crown area corresponded to about 45% of the total cylinder bore area. The flame area shown in the graphs is only accurate for quantitative interpretation of the differences between fuels only while the flame remained within the optical piston crown area. Typically, flame clipping by the boundaries of the piston crown window started at roughly the 30% mark (corresponding to ~14 mm equivalent flame radius) between ~20–25 °CA AIT, as indicated by the dashed horizontal line in the flame area graph of **Figure 9**. The respective mass fraction burned at the clipping point was below 5%. For any curve comparisons later in the flame growth process, *i.e.* past the nominal window clipping limit, it has to be considered that some flames, especially those of ethanol, were associated with a more centralised flame kernel growth and rounder flame than the other fuels, so that the occupied window area would increase more than for a fuel which had a higher percentage of enflamed area clipped by the optical boundary. Ethanol showed the fastest flame area growth and reached the clipping point about 4 °CA earlier than butanol, whilst *iso*-octane was clearly the slowest. The standard deviation was at its highest at about 55% of the optical window area for all fuels, with values ranging from about 8% to 18% for the different fuels.

These observations were broadly in agreement with heat releases analysis of the simultaneously acquired in-cylinder pressure records. An initial 'ignition delay' for all fuels was calculated from the flame images by appropriately distinguishing the bright area occupied by the spark from that of the flame's chemiluminescence in the early crank angles of growth. Typical values in the range of 5–7 °CA were quantified. Those delay values were lower than those derived from MFB analysis, showing the sensitivity advantage of the optical analysis; the pressure traces started to exceed the motoring compression pressure in the region of 12–16 °CA AIT. For reference, 10% MFB occurred in the region of 30–40 °CA AIT (ethanol fastest, *iso*-octane slowest) and very little differences could be resolved between fuels at MFB values below 2–3% MFB due to the typical response issues of in-cylinder pressure transducer diagnostic techniques.

Flame Tomography Probability of Flame Presence

The probability of flame presence from the flame tomography images is shown in **Figure 10** for the four fuels and with four different Laser pulse separations, specifically 10, 25, 50 and 100 μs; to bring these values into context it is noted that 1 °CA corresponded to ~111 μs. A circle has been superimposed on each one of the 1st row images to indicate the outlining of the spark plug for reference. 100% probability is represented by dark red, *i.e.* indicating that this pixel was within the flame boundary of all images of the set, whilst 0% probability is given in dark blue for a pixel always outside the flame boundary. The second frame of each image pair was employed for this analysis; therefore, slightly larger areas of non-zero probability can be seen with the largest pulse separation of 100 μs. These images confirm the tendency of the combustion to propagate in the direction of the exhaust valves, typically carried by the tumble flow motion. Flames were elongated along the pent-roof axis (as also observed in the flame chemiluminescence images), more so for gasoline than for the other fuels.

Figure 11 shows the average flame area and equivalent flame radius quantified from the first image frame, with the standard deviations superimposed as error bars for all fuels. Gasoline's flame radius was 9.1 mm, approximately 15% and 7% smaller than ethanol's and butanol's radius respectively, even though gasoline's

image capture corresponded to 1 °CA later than that of both alcohols. *Iso*-octane's average flame radius was 10.3 mm, roughly halfway between the two alcohols, yet its image capture had been delayed by 3 °CA (18 °CA AIT *vs.* 15 °CA AIT); *iso*-octane's measurements showed a quite small flame radius of about 5–6 mm when captured at 15 °CA AIT. Considering that the integral length scale on the swirl plane at ignition timing was of the order 5–6 mm, flames of radii 9–10 mm corresponded to flames that had grown to size of ~3.5 integral length scales. It is also noted that, on the estimate of spherical expansion, the flames occupied ~5–10% of the combustion chamber's volume at the time of measurement, without excluding the spark-plug's volume, *i.e.* even smaller than 5–10% volume fraction burned in realistic terms. Heat release analysis for all fuels showed that the mass fraction burned at their respective image timings of 15–18 °CA AIT was not more than ~1%.

Figure 12 shows the flame speed against pulse separations of 10, 25, 50 and 100 μs, as calculated by the growth in equivalent flame radius from one Laser pulse to the next. For comparison, the integral timescale quantified by LDV in the same engine at the same conditions was about 1–2 ms [55]. An advantage of small pulse separations was that the flow field could also be obtained by PIV in the unburned charge. Additionally, superimposed effects such as flame convection or 'out-of-plane flame fingers' propagating into the Laser plane were weaker with small separations. It is likely that the different trend seen between the alcohols and the hydrocarbon fuels when the Laser pulse separation was increased from 10 μs to 25 μs was due to the limited spatial resolution of the flame's growth rate. Specifically, with a resolution of 33.4 μm/pixel and at a speed of 9.5 m/s, the corresponding effective time resolution would be ~3.5 μs, *i.e.* just 1/3rd of the 10 μs separation. However, a general trend of larger flame radius growth rates could be seen for both alcohol fuels compared to *iso*-octane and gasoline, with ethanol being significantly fastest than all fuels from pulse separations of 25 μs onwards.

Flame Speed and Roundness

In order to get information about the flame propagation for various flame sizes, the measurement results for the pulse separations of 25–100 μs were grouped in bins with a width of 2 mm, overlapping by 1 mm (*e.g.* the 7 mm bin includes radii between $6<r<8$ mm, overlapping with the 8 mm bin with $7<r<9$ mm). Very few cycles were found with flame radii below 6 mm and beyond 16 mm for all fuels, with gasoline showing more small flames than the others. Flames will radii between 8–12 mm had about 40–50% probability of occurrence for all fuels. Sorting flames into three radii bins from 9–11 mm resulted in each fuel having per bin about 17–20% of the total population of flames per batch. The left graph in **Figure 13** shows the flame speed for each one of the four fuels for these three radii bins along with the standard deviation as error bars. The right graph contains the average flame speed when all flames of radii between 8–12 mm were brought together for each fuel. These two graphs also contain the results from the same type of exercise on the chemiluminescence images in lighter equivalent colouring. The values derived from the flame tomography data show that ethanol had the highest flame speed, about 10% faster than butanol and ~15% faster than gasoline. These trends are broadly in agreement with the chemiluminescence data, albeit the average velocities obtained from tomography were distinctly lower by 13–17% than those of the flame chemiluminescence imaging at the same flame radius throughout all fuels. However, *iso*-octane shows a clear discrepancy in trends between the two techniques when compared to gasoline. Specifically, *iso*-

octane's flame speed was always smaller than gasoline's in the chemiluminescence-derived data set, but it was larger in the tomography-derived data set. This observation was examined closely and it was concluded that it was associated with real effects of the planar flame morphology of the two fuels. Gasoline's batch of tomographic images exhibited increased presence of flame clustering from out of plane 'finger' contributions to unburned gas holes, as further discussed later.

The flame speed appeared only weakly dependent on flame size within the set of 8–12 mm radii of flame tomography data, with only ethanol and butanol showing a small increase in radius growth speed for larger flame radii. This degree of independence became more obvious when the measured flame speed of all individual cycles was compared to the respective radius data. Mostly ethanol and butanol showed a positive trend with increasing flame radius; however, the spread was large resulting in correlation coefficients of 0.17 for ethanol and 0.14 for butanol (correlation coefficients close to zero were calculated for gasoline and *iso*-octane). This suggested that the increase in velocity seen from chemiluminescence (typically ~10% between 8 to 12 mm flame radius) may be dominated by other factors of bulk 3D nature. To bring these data in the context of flame stretch, a measure of stretch caused by curvature can be calculated from the flame speed data shown in **Figure 13** and the radii of **Figure 11**. This can be done by considering the stretch that would be experienced by a sphere of that size and speed, *i.e.* $(2/r)(\mathrm{d}r/\mathrm{d}t)$. In this context, stretch rates of ~2,000 s^{-1} were calculated for both alcohols and gasoline, whilst *iso*-octane was associated with ~10% lower stretch. When compensating for the gas expansion by dividing the measured flame speed by the ratio of unburned to burned gas densities, a turbulent burning velocity of 2.23 m/s emerged for ethanol, 2.05 m/s for butanol, 2.00 for *iso*-octane and 1.94 m/s for gasoline at their respective sizes.

The results of the flame roundness analysis can be found in **Figure 14** in the left graph for the three radius bins of 9, 10 and 11 mm and on the right as averaged value over radii 8–12 mm. On this parameter, tomography and chemiluminescence agree in terms of trends between fuels, with ethanol showing the roundest flames of all fuels and *iso*-octane the least round (~20% lower roundness than ethanol). Butanol's roundness was ~8% below ethanol's and in turn gasoline's ~8% below butanol's. The roundness dependency on flame radius showed a positive correlation throughout all fuels with a large spread in individual flames leading to correlation coefficients were low with 0.24 for ethanol, 0.10 for butanol, 0.04 for gasoline and 0.13 for *iso*-octane. The roundness values of the chemiluminescence analysis were much larger, about 18–25%, due to the global representation of the flame shape.

To put the fuels and in-cylinder conditions of the present study into the context of combustion diagrams and modelling, *e.g.* see Bradley [68] and Peters [70], various combustion parameters are shown in **Table 6** for both alcohols and *iso*-octane; gasoline was not evaluated due to lack of known values for all its thermophysical properties. Selection of turbulence intensity values u' is not always straightforward for such an exercise in real engines. Statistical analysis of in-cylinder flow velocities by both LDV and PIV methods in the engine under study showed u' values of the order 3.0 m/s on the basis of typical ensemble averaging techniques that lead to 'mean' and 'RMS' values [54, 55]. However, methods to distinguish in-cycle bulk velocities from high-frequency turbulence values were also applied to the LDV data of the current engine according to [71] and these led to u' values of ~1.5 m/s [55]. The laminar burning velocities of [40, 41] at 5 bar, 423 K were used as baseline, whilst all the other parameters were calculated for 5 bar, 500 K, the

approximate pressure and temperature at ignition as obtained from the engine's pressure traces. The resultant values placed the regime of combustion close to the boundary between corrugated flamelets and distributed reactions as shown in the Peters-Borghi diagram of **Figure A1** in the **Appendix** for 1.5 and 3 m/s turbulence intensity. The residual gas fraction was not included in the calculation of laminar burning velocities due to lack of purposely derived correlations on the effect of residuals for all these fuels at the same conditions of temperature and pressure. However, the residual gas fraction was estimated at about 8% at the conditions of study and this is expected to decrease the laminar burning velocities by about 30% according the work of [41] on *iso*-octane and ethanol fuels and of [72] on *iso*-octane and *n*-butanol blends. The reader is also guided to [53] where dilution effects have been discussed by in-cylinder flame tomography imaging and reference to the Peters-Borghi diagram in an engine of similar geometric characteristics to that of the current study, as well as to [51] for a similar discussion on both diagrams through chemiluminescence analysis of data from a another engine of analogous geometry.

Flame Front Wrinkling Frequencies

Figure 15 contains typical flame contours, small, medium and large flames; all correspond to ethanol. Each chart contains the raw flame contour of the second image frame in blue and the filtered mean contour in red. The geometrical flame area's centroid is marked with a red cross. Resulting crests with the raw flame exceeding the filtered boundary are highlighted in green, while cusps regions with the raw flame within the filtered boundary are in yellow. The spark plug gap is located at z=33.4 mm (horizontal), y=-38.3 mm (vertical) and the cylinder's centre at z=33.4 mm, y=-34.8 mm. Very small flames below 4 mm in radius were very rare, especially for ethanol which showed such small radii in only 0.5% of the cycles, while the other fuels in ~1.5% of the cycles. The majority of flames were in the medium to large range, 8–14 mm.

One difference that became obvious when inspecting the raw flame images of all fuels was that *iso*-octane and more so gasoline were exhibiting more clustered flame structures with multiple islands of flame kernels than both alcohols. It is believed that these flame kernels were not truly independent but they were connected to a single global flame structure above and/or below the Laser sheet, therefore the recorded flame clustering was a manifestation of flame 'fingers' protruding into the image plane. Approximately 20% of all hydrocarbon flames showed such clustered structures with two or more flame regions, with gasoline the most affected, whilst the respective occurrence for the alcohol fuels was less than 10%. An example of such clustered flame structures is also presented in **Figure 15**. Flame images with such degree of fragmentation were excluded from the analysis presented hereafter and form part of a separate study that will be discussed in the future. The reader is also guided to [42] for a discussion on the challenges of calculating turbulent burning velocities.

The Fourier transformation of the developed flame contour allows for the quantification of the length scale of the wrinkles in the flame front, as shown exemplary for an individual image in the left graph in **Figure 16**. The right graphs show the averaged Fourier transforms of all fuels and images. Ethanol was showing largest fluctuation amplitudes (=wrinkle height), followed by *iso*-octane, which had slightly higher amplitudes than butanol especially towards higher frequencies (=smaller wrinkle length) and finally gasoline which had the smallest average wrinkle amplitudes. Analysis of the Fourier transform of individual images showed that highest wrinkle amplitudes were returned for frequencies between about 0.05–0.6 mm^{-1}, translating into sizes

of 1.5–20 mm with the maximum typically found between 0.10–0.14 mm^{-1}, *i.e.* sizes of 7–10 mm. The maximum size scales were therefore approximately twice that of the largest integral length scales of turbulence at the time of ignition found in the swirl view and which were up to 10 mm. The average integral length scales on the swirl plane were 4–7 mm, *i.e.* the dominating flame tomography scales of 7–10 mm were approximately 40–70% larger than the average integral length scales of turbulence. Considering the later timing of flame image acquisition than the ignition timing where the integral length scales were quantified at, and on the informed assumption that the integral length scales of turbulence typically reduce in size with the reduction in clearance height past ignition timing, it can be noted that the half periods of the frequencies visible in the flame outlining were close to the integral length scales of turbulence, *i.e.* eddies with a diameter of the integral length scale fit into the half wave created by a half sinus, *i.e.* between the largest crests and cusps of the flame's wrinkles.

Calculating the standard deviation of the displacement of the flame's instantaneous contour from the filtered contour, denoted by σ_d, quantifies an average wrinkle amplitude that can be used as a measure of the turbulent flame thickness. Average values of 0.54 mm for ethanol, 0.47 mm for butanol, 0.51 mm for *iso*-octane and 0.43 mm for gasoline were obtained. A strong correlation can be seen for all fuels between this measure of flame thickness and the flame's radius in either absolute or normalised form in **Figure 17**. The normalised flame brush thickness σ_d/r was of the order 4–6% over the range of flame radii measured. This appears in general fairly independent of fuel type. However, upon close inspection it is clear that the ethanol flames carried a smaller σ_d/r for their size (*i.e.* a thinner flame brush for their size) and that *iso*-octane's flames were associated with a much wider range of σ_d/r and with some small flames carrying the thickest flame brush. This behaviour can be linked to the fact that ethanol flames were rounder and *iso*-octane's flames the least round as discussed earlier.

The current investigation also showed that smaller numbers of crossing points between the instantaneous and filtered contours correlated with larger equivalent flame radii and σ_d, as shown in **Figure 18** (*i.e.* thicker flame fronts correlated with fewer crossings). The mean number of crossing points per mm was 0.7 for ethanol, 0.8 for butanol, 0.85 for gasoline and 0.73 for *iso*-octane (with respective standard deviations of 0.1, 0.11, 0.15 and 0.21). This analysis would suggest that cycles that were subjected to predominantly larger scale eddies (*i.e.* resulting in a smaller number of crossing points and stronger wrinkling) were leading to faster combustion than cycles with smaller length scales of turbulence. However, there was no correlation between the crossing point frequency and the equivalent flame speed. It is therefore more likely that the larger flames simply allow interaction of the flame front with larger scale eddies, with those eddies having predominantly a convective or large-scale distortion effect (*e.g.* see [68]) which can be matched by the filtered mean contour on smaller flames. While the current study showed crossing frequencies between 0.5–1.3 mm^{-1} for flame radii between 2–18 mm, with average flame propagation speeds of 9–11 m/s, chemiluminescence flame imaging analysis has shown frequencies between 0.1–0.5 mm^{-1} at lean and 0.15 mm^{-1} at stoichiometric AFR for *iso*-octane fuel [66]; this could be due to masking effects of smaller wrinkles by the projected along the line of sight nature of the chemiluminescence imaging technique (*i.e.* in the same way sharp peaks are masked along a ridge of mountains). The FFT data presented in **Figure 16** showed strongest peaks at low frequencies of 0.1 mm^{-1}, what would correspond to a crossing frequency of 0.2 mm^{-1}.

While the amplitude effect is neglected in the crossing point analysis, the FFT takes it into account, highlighting the stronger wrinkle amplitudes for lower crossing frequencies (*i.e.* large wrinkles are high and wide). The range of average crossing frequencies for each cycle, 0.5–1.3 mm^{-1}, also showed strong amplitudes in the corresponding FFT range of 0.25–0.65 mm^{-1}; however, the extremities of the FFT, including the strongest peak location, were not represented in the crossing point analysis.

The flame thickness σ_d and the crossing point frequency of the four fuels are plotted against the integral length scales in **Figure 19**. The length scales obtained from the tumble plane are illustrated in light blue colour, those form the swirl plane in dark blue, and the average value of both planes in red. There is clearly a positive correlation, indicating that the larger eddies will create deeper wrinkles and a thicker flame front. Accordingly, as the scales get larger, the number of crossings per mm reduces. There is also clearly one order of magnitude difference between σ_d and mean integral length scales, highlighting that flame front wrinkles are in size ~$1/10^{th}$ of the integral length scale. Gasoline showed the largest deviation from these trend lines probably due to its smaller flame size that had not been affected by the integral length scales in the same turnover manner during the studied timescale of flame growth, or because of the presence of more fragmented flame structures with this fuel.

Flame Front Crest and Cusp Velocities

The Lewis number *Le*, which relates the thermal diffusivity to the mass diffusivity of the deficient reactant in the inert (nitrogen), is typically used to estimate the extent of non-equidiffusivity. For lean mixtures, the deficient reactant is the fuel, while rich mixtures are limited by the available oxygen. Flames with Lewis numbers greater than unity (heat loss due to high thermal diffusivity greater than deficient reactant mass transfer into the reactive region) are considered to have a stabilising effect on the flame front. For such cases, a laminar spherical flame that develops starts off as highly stretched (small radius) and the flame gets faster with the increase in radius, with the resulting negative of the gradient being known as the Markstein length. Flames with such behaviour would counteract stretch effects on the flame front, suppressing instabilities. In contrast, Lewis numbers smaller than unity (deficient reactant mass transfer greater than heat transfer) are susceptible to intensify instabilities, as the flame speed increases for stronger stretched regions and the velocities at the crests of flame wrinkles should be higher than at the cusps. More details on the calculation of the Lewis number and its effect on laminar and turbulent flame speeds can be found in [73–78]. For calculating the Lewis number of the single component fuels used in this study (ethanol, butanol and *iso*-octane) and at the engine's thermodynamic conditions at ignition timing, values of specific heats, thermal conductivity, density and viscosity of the mixtures, as well as diffusion coefficients, were required. These were taken from [79–81]; gasoline was exempted from this exercise due to lack of all necessary thermophysical properties. The binary diffusion coefficient for *Le* was based on either oxygen or the fuel as deficient reactants to produce 'lean' and 'rich' values, while the equivalent 'stoichiometric' value was based on the average of these two values following the methodology adopted by Bradley and co-workers [73–76]. The calculated values were also compared to values in the literature for a range of fuels, *e.g.* [82, 83], with very good agreement. The Lewis numbers at lean/rich were finally obtained as 1.50/0.92 for ethanol, 2.12/0.91 for butanol and 2.79/0.92 for *iso*-octane, with average values 1.21, 1.52 1.86, respectively. According to this, *iso*-octane would have best stabilising capabilities against thermo-diffusive instabilities,

followed by butanol and lastly ethanol. As lower Lewis numbers are known to increase the flame speed for increased flame stretch, ethanol's low Lewis number may contribute to its significantly faster flame development in the early, highly stretched phases of the combustion. This effect reduces with the reducing stretch during ongoing near spherical flame growth, what would provide an explanation for the larger flame diameters of ethanol at the time of measurement compared to butanol, considering similar unstretched laminar flame speeds. The even smaller flames of *iso*-octane, having the largest Lewis number, would also support this.

Figure 20 illustrates examples of calculation of the local flame speed at crests and cusps for larger-sized flames (pulse separation 25 µs). The filtered flame contours are shown as black dashed lines for frame A and dash-dotted for frame B. The outlining of the instantaneous flames is red and blue for frames A and B, respectively. The velocity vectors are shown in light red for crests and light blue for cusps. When averaging the respective vectors within one image and taking the mean over all cycles returned average crest velocities of 7.30 m/s for ethanol, 7.05 m/s for butanol and *iso*-octane and 6.62 m/s for gasoline. The cusp velocities were 7% lower for ethanol (6.80 m/s), 10% lower for butanol (6.35 m/s), 8% lower for *iso*-octane (6.55 m/s) and 7% lower for gasoline (6.18 m/s). The higher velocities at the crests, *i.e.* positively stretched regions, compared to the negatively stretched cusp regions may be the indicator of thermo-diffusive instabilities which occur for Lewis numbers smaller than unity. Fuel rich regions with oxygen as the deficient reactant fulfil this condition hence issues related to the degree of mixture inhomogeneity in practical engine environments requires further study. The cylinder charge of this engine has not been investigated regarding locally rich or lean regions at the spark plug at ignition timing. However, AFR variations were likely and would also vary with fuel type as shown by [50] for the same fuels in an optical engine of very similar geometry and capacity to that of the current study (typically $\pm 0.05\phi$ among fuels).

The increasing σ_d for increasing flame radii could therefore be at least partly a result of the crest-cusp velocity difference, as well as an effect of the larger scale turbulence structures interfering with the flame front for larger sized flames. This becomes more obvious when looking at the growth in flame thickness by ~0.28 mm between flame radii from 6–12 mm (**Figure 17**). The growth in wrinkle height by 0.28 mm would require a crest-cusp velocity difference of ~0.56 m/s over 4.5 °CA (time necessary for a flame to grow from 6 to 12 mm as by chemiluminescence imaging). Only *iso*-octane did not get close to this value. The average flame front velocity combining cusps and crests was highest for ethanol with 7.0 m/s, followed by *iso*-octane with 6.81 m/s, butanol with 6.76 m/s and lastly gasoline with 6.48 m/s. Considering the turbulence intensity in the vicinity of the spark plug at ignition timing, the flame speed was of the order 2–3u'. Relating the speed of the flame front S_{front} to the flame's equivalent radius growth rate S_{equ}, suggests a linear relationship within the given flame speed range:

$$S_{equ} = 3.39 S_{front} - 13.55$$

with a coefficient of determination R^2 of 0.95 (considering that the trend line needs to pass through the point S_{equ}=S_{front}=0, the suggested relation can only be a local gradient).

Fast flame speeds at the flame front did not always correlate with higher equivalent radius growth rates for individual cycles. This is believed to be due to flame area growth effects within the flame boundary, where inclusions of unburned mixture are consumed. The average trend is however clearly showing the expected

trend. The stated average flame front velocity values do not account for the radius differences and therefore graphs are shown for each fuel giving the instantaneous flame front's crest and cusp velocities against flame radius in **Figure 21**, with the crest velocity in red and the cusp velocity in blue. The graphs show a strong variation around the trend lines, more so for the hydrocarbon fuels. All four fuels showed similar velocities of 7.0 m/s for crest and 6.4 m/s for cusp regions for a flame radius of 10 mm, while butanol showed the highest trend line gradient and highest correlation with flame radius, followed by ethanol, gasoline and lastly *iso*-octane. For spherical laminar flames, higher gradients in the trend line would indicate better flame stabilisation due to higher velocities with reduced stretch due to flame radius growth. However, in the current turbulent case, this is counteracted by the stronger stretch from increased wrinkling for larger flame radii.

Flow Velocity in the Vicinity of the Flame Front

Extraction of the velocity field in the unburned mixture of in the tomography data followed the PIV approach described in earlier section. Data with a Laser pulse separation of 10 μs were analysed. The main interest within the objectives of the current paper was not the overall flow field in the unburned charge but the velocities of the charge at the flame boundary. **Figure 22** shows an ethanol flame with superimposed the velocity field in the unburned charge and the extracted velocity vectors just upstream the flame front. The magnitude of velocity was then averaged along the flame outlining to obtain a mean value and further averaged over all flames for each fuel.

The charge velocity at the flame front was expected to be dominated by the flame expansion speed caused by the density difference between burned and unburned gases, as can be seen in individual vector fields where the 'normal' velocity field without combustion was no longer present. Some contribution of the initial flow-field such as turbulence and bulk motion components could still be present and it may not be fully appropriate to subtract the unburned charge velocity just in front of the flame front from the measured flame speed in order to obtain a turbulent burning velocity (including some contribution of flame convection). However, it may be used as a first approximation to be compared with the results obtained when the flame expansion speed was divided by the density ratio of unburned to burned gases. The reader is referred to publications by Bradley and co-workers for further details on the contributions of curvature and strain to the burning velocity, *e.g.* see [68].

The results of the analysis have shown average unburned charge velocity magnitudes at the flame front location of 7.8 m/s for ethanol, 7.6 m/s for gasoline as well as 7.1 m/s for butanol and *iso*-octane with standard deviations between 1.4–1.9 m/s. Using those velocities and respective flame radii, one can estimate the stretch caused by aerodynamic strain as high as ~1700 s^{-1} for gasoline, *i.e.* of the same order to that estimated from curvature effects, and as low as ~850 s^{-1} for ethanol. Subtracting the unburned charge velocity values from the respective flame speed data obtained earlier, ethanol would return 2.7 m/s, butanol 2.5 m/s, *iso*-octane 2.3 m/s and gasoline 1.5 m/s. For comparison, the values of turbulent burning velocity calculated by conventional division of the average flame expansion speed by the density ratio of unburned to burned gas were 2.23 m/s for ethanol, 2.05 for butanol, 2.00 for *iso*-octane and 1.94 for gasoline. The values of ethanol, butanol and *iso*-octane appear reasonably good in terms of trends, with an overall velocity magnitude ~15% larger than with the conventional approach. To match values, a burned to unburned density ratio of 3.9 would have to be assumed for the alcohols and 4.1 for *iso*-octane. Gasoline shows larger

difference between the two methods though and it would require a density ratio of 6.1 for a match. Considering that such a density ratio is excessive at these conditions, it seems that there are other mechanisms involved in the case of gasoline. This also appears in agreement with the fact that gasoline was furthest away from the correlation line between integral length scale and σ_d or crossing frequency in **Figure 19**. Gasoline's discrepancy is believed to be linked to its smaller flame size morphology and higher stretch. Increased optical resolution would be beneficial in future experiments to decouple associated effects in more detail.

SUMMARY AND CONCLUSIONS

The current paper presented results from an optical study of stoichiometric combustion of gasoline, *iso*-octane, ethanol and *n*-butanol fuels in a direct-injection spark-ignition engine. The engine speed was 1500 RPM with 0.5 bar intake plenum pressure and 80 °C engine coolant temperature. The spark advance was 25 °CA for all fuels. Analysis involved results from three types of optical experiments: PIV of the in-cylinder flow field at ignition timing without fuelling (*i.e.* air only) and with fuel injection strategy in the early intake stroke (for homogeneous mixture preparation), crank-angle-resolved flame chemiluminescence imaging to characterise the global behaviour of the flame, and double-pulsed Laser-sheet flame tomography to quantify the local topology of the flame front. The main conclusions of this study can be summarised as follows:

- The flow field without fuel injection showed mean velocities between 3–5 m/s from intake to exhaust on the tumble plane with turbulent kinetic energy between 9–15 m^2/s^2. Two counter rotating swirl vortices were observed on the horizontal plane with their centres below each one of the intake valves; maximum velocities were again up to 5 m/s and turbulent kinetic energy between 9–16 m^2/s^2.
- Fuel injection in the intake stroke led to relatively small differences in the bulk flow bulk structures at ignition timing when compared to air only motoring conditions. However, maximum velocities were ~10% higher for gasoline and ~30% lower for butanol, with ethanol and *iso*-octane cases in-between. The turbulent kinetic energy on the tumble plane was highest on the exhaust side of the engine for air only motoring, but fuelled cycles showed highest values on the intake side (up to ~18 m^2/s^2).
- Integral length scales without fuel injection were for the tumble view 2–4.5 mm in the vertical direction (*i.e.* along the piston's motion) and 4–7 mm in the horizontal direction (*i.e.* across the bore from inlet to exhaust). The swirl plane view showed length scales between 4–10 mm. In non-dimensional form, integral scales were up to 20% of the clearance height and 5–12% of the cylinder bore.
- The integral length scales with fuel injection were of the same order of magnitude to those of air only measurements on the tumble plane, but showed distinctly larger regions with length scales up to 9 mm on the swirl plane. Differences between fuels were small, with average scales on both planes between 4–6 mm. Ethanol was typically associated with largest scales and butanol with smallest.
- When comparing the tomography images of all fuels at similar flame radii between 8–12 mm, ethanol was fastest with speeds of 10.5 m/s, butanol second fastest with 9.6 m/s, followed by *iso*-octane and gasoline with 9.4 and 9.1 m/s, respectively. The results were 13–20% lower than those obtained from chemiluminescence imaging, highlighting planar effects in comparison to global visualisation.

- Using the ratio of unburned to burned gas density, turbulent burning velocities of 2.23 m/s emerged for ethanol, 2.05 m/s for butanol, 2.00 for *iso*-octane and 1.94 m/s for gasoline. These were 4.6–6.5 larger than laminar burning velocity values in the literature at similar thermodynamic conditions.
- The flame speed obtained from tomography was fairly independent of the equivalent flame radius within the range of sizes studied, but chemiluminescence showed increased flame speed with larger flame sizes.
- The flame roundness was ~10–15% from tomography images, with largest values for ethanol, then for butanol, gasoline and finally *iso*-octane. This reflects the fact that the hydrocarbon fuels exhibited more often multiple flame clusters and stronger flame distortion. The chemiluminescence images showed same order of roundness in terms of fuel sequence but with levels of ~18–25%.
- Fourier transformation of the instantaneous flame contours showed similar traces for all fuels with maximum amplitudes at 0.10–0.14 mm^{-1}, *i.e.* periods of 7–10 mm. These were approximately 1.4–2 times the integral length scale.
- Increasing wrinkled depth was observed with increasing flame size. The standard deviation of the displacement of the instantaneous flame contour from one filtered by its equivalent radius (σ_d) was obtained as a measure of the flame brush thickness (*i.e.* size/depth of wrinkles) and correlated strongly with the equivalent flame radius, independently of fuel type. Average values of 0.54 mm for ethanol, 0.51 mm for *iso*-octane, 0.47 mm for butanol and 0.43 mm for gasoline were obtained. When the flame brush was normalised by the equivalent flame radius, values of 4–6% were obtained for all fuels.
- The number of crossing points between instantaneous and filtered flame contours showed a strong negative correlation with flame radius, independent of fuel type (correlation coefficient of ~0.85). The typical crossing point frequency range was between 0.5–1.6 mm^{-1}.
- The flame brush thickness was ~$1/10^{th}$ of the integral length scale. The average integral length scales showed a positive correlation with the flame brush thickness and a negative correlation with the crossing point frequency (correlation coefficients of ~0.6).
- The average local flame front speed was calculated by the tomography contours to be 2–3u'. Analysis of the average flame crest velocities returned values of about 7.30 m/s for ethanol, 7.05 m/s for butanol and *iso*-octane and 6.62 m/s for gasoline. The cusp velocities were lower by 7% for ethanol, 11% for butanol, 8% for *iso*-octane and 7% for gasoline. Considering that the average Lewis numbers of these fuels were greater than unity, larger velocities were expected at the cusps. However, for rich mixtures the Lewis number was ~0.9 for all fuels which could help explain the measured crests/cusps velocity differences in view of local equivalence ratio departure from stoichiometry around the spark plug.
- The turbulent burning velocity was also calculated by subtraction of the unburned charge velocity at the flame front from the flame's expansion speed. For both alcohols and *iso*-octane, the resultant values were ~15% larger than those obtained by accounting for the density ratio of unburned to burned gas. Gasoline showed larger difference between the two methods. This appears in agreement with the discrepancy of gasoline being furthest away from a correlation line between integral length scale and σ_d or crossing frequency and may be linked to gasoline's higher stretch by both curvature and aerodynamic effects.

Current work is focused on planar Laser-induced fluorescence contours of OH [84–86] using similar processing methodologies to those of the Mie-scattering tomography technique discussed here. The

outcomes will offer an informative comparison of the two approaches, including flame stretch and Markstein effects. Additionally, comparison of port fuel injection and direct injection with the same fuels over a range of equivalence ratios will shed more light onto mixture preparation effects on the in-cylinder flow at ignition timing and flame front characteristics, especially with crank-angle resolved imaging. In this context, it is also of interest to understand the effect of mixtures that may still carry fuel droplets. For example, *iso*-octane aerosols in combustion-bomb experiments have shown that existence of micron-size droplets in the mixture field can affect burning rates significantly at laminar conditions but the effect is quickly negated by turbulence and can become insignificant at typical in-cylinder levels of turbulence intensity [87, 88]; however, no data exist with lower volatility or higher latent heat fuels like butanol and ethanol, respectively.

ACKNOWLEDGMENTS

The authors would like to thank Dave OudeNijeweme and Paul Freeland of MAHLE Powertrain, Ltd., UK for financial and technical support.

APPENDIX

Peters-Borghi Diagram.

REFERENCES

1. Kabasin, D. F., Hurter, T., Lamers, R., Hoyer, K. and Kazour, J., "Heated Injectors for Ethanol Cold Starts", SAE Paper 2009-01-0615, 2009.
2. Brinkman, N. D., "Ethanol Fuel – A Single Cylinder Engine Study of Efficiency and Exhaust Emissions", SAE Paper 810345, 1981.
3. Gautam, M. and Martin D. W., "Combustion Characteristics of Higher Alcohol/Gasoline Blends", Proceeding of IMechE, Part A, Journal of Power and Energy, Vol. 214, pp. 497–511, 2000.
4. Davis, G. W. and Heil, E.T., "The Development and Performance of a High Blend Ethanol Fueled Vehicle", SAE Paper 2000-01-1602, 2000.
5. Al-Farayedhi, Al-Dawood, A. M. and Gandhidasan, P., "Experimental Investigation of SI Engine Performance Using Oxygenated Fuel", Transactions of ASME, Journal of Engineering for Gas Turbines and Power, Vol. 126, pp. 178–191, 2004.
6. Nakata, K., Utsumi, S., Ota, A., Kawatake, K., Kawai, T. and Tsunooka, T., "The Effect of Ethanol on a Spark Ignition Engine", SAE Paper 2006-01-3380, 2006.
7. Topgül, T., Yücesu, H. S., Cinar, C. and Koca, A., "The Effects of Ethanol-Unleaded Gasoline Blends and Ignition Timing on Engine Performance and Exhaust Emissions", Renewable Energy, Vol. 31, pp. 2534–2542, 2006.
8. Guerrieri, D. A., Caffrey, P. J. and Rao, V., "Investigation into the Vehicle Exhaust Emissions of High Percentage ethanol Blends", SAE Paper 950777, 1995.
9. Gautam, M., Martin, D. W. and Carder, D., "Emissions Characteristics of Higher Alcohol/gasoline Blends", Proceedings of IMechE, Part A, Journal of Power and Energy, Vol. 214, pp. 165–182, 2000.
10. Sandiquist H., Karlsson, M. and Denbratt, I., "Influence of Ethanol Content in Gasoline on Speciated Emissions from a Direct-Injection Stratified Charge SI Engine", SAE Paper 2001-01-1206, 2001.
11. Martinez, F. A. and Ganji, A. R., "Performance and Exhaust Emissions of a Single-Cylinder Utility Engine Using Ethanol Fuel", SAE Paper 2006–32–0078, 2006.

12. Szwaja, S., Naber, J. D., “Combustion of *n*-Butanol in a Spark-Ignition Engine”, Fuel, Vol. 89, pp. 1331–1748, 2010.
13. Malcolm, J. S., Aleiferis, P. G., Todd, A. R. and Cairns, A., Hume, A., Blaxill, H., Hoffmann, H. and Rueckauf, J., “A Study of Blended Alcohol Fuels in a New Optical Spark-Ignition Engine”, Proceedings of International Conference on Internal Combustion Engines: Performance, Fuel Economy and Emissions, IMechE, London, pp. 223–234, 2007.
14. Todd, A., Fraser N., Aleiferis, P. G., Malcolm J. and Cairns, A., “A Study of Alcohol Blended Fuels in an Unthrottled Single-Cylinder Spark-Ignition Engine”, SAE Paper 2010-01-0618, 2010.
15. Cairns, A., Zhao, H., Todd, A. and Aleiferis, P. G., “A Study of Mechanical Variable Valve Operation with Gasoline-Alcohol Fuels in a Spark-Ignition Engine”, Fuel, Vol. 106, pp. 802–813, 2013.
16. Merola, S., Tornatore, C., Valentino, G., Marchitto, L. and Corcione, F., “Optical Investigation of the Effect on the Combustion Process of Butanol-Gasoline Blend in a PFI SI Boosted Engine”, SAE Paper 2011-24-0057, 2011.
17. Tornatore, C., Merola, S., Valentino, G.and Marchitto, L., “In-Cylinder Spectroscopic Measurements of Combustion Process in a SI Engine Fuelled with Butanol-Gasoline Blend”, SAE Paper 2013-01-1318, 2013.
18. Zhu, G., Stuecken, T., Schock, H., Yang, X., Hung, D. and Fedewa, A., “Combustion Characteristics of a Single-Cylinder Engine Equipped with Gasoline and Ethanol Dual-Fuel Systems”, SAE Paper 2008-01-1767, 2008.
19. Aleiferis, P. G., Malcolm, J. S., Todd, A. R., Cairns, A. and Hoffmann, H., “An Optical Study of Spray Development and Combustion of Ethanol, *iso*-Octane and Gasoline Blends in a DISI Engine”, SAE Paper 2008-01-0073, 2008.
20. Aleiferis, P. G., Serras-Pereira, J., van Romunde, Z., Caine, J. and Wirth, M., “Mechanisms of Spray Formation and Combustion from a Multi-Hole Injector with E85 and Gasoline”, Combustion and Flame, Vol. 157, pp. 735–756, 2010.
21. Smith, J. D. and Sick, V., “The Prospects of Using Alcohol-Based Fuels in Stratified-Charge Spark-Ignition Engines”, SAE Paper 2007-01-4034, 2007.
22. Wallner, T., Miers, S.A. and Mconnell, S., “A Comparison of Ethanol and Butanol as Oxygenates Using a Direct-Injection, Spark-Ignition Engine”, Transactions of ASME, Journal of Engineering for Gas Turbine and Power, Vol. 131, pp. 032802-1–032802-9, 2009.
23. Merola, S., Marchitto, L., Tornatore, C., Valentino, G. and Irimescu, A., “UV-visible Optical Characterization of the Early Combustion Stage in a DISI Engine Fuelled with Butanol-Gasoline Blend”, SAE International Journal of Engines, Vol. 6, pp. 1953–1969, SAE Paper 2013-01-2638, 2013.
24. Gülder, Ö. L., “Burning Velocities of Ethanol–*iso*-Octane Blends”, Combustion and Flame, Vol. 56, pp. 261–168, 1984.
25. Gülder, O. L., “Correlations of Laminar Combustion Data for Alternative SI Engine Fuels”, SAE Paper 841000, 1984.
26. Metghalchi, M. and Keck, J. C., “Burning Velocities of Mixtures of Air with Methanol, *iso*-Octane and Indolene at High Pressure and Temperature”, Combustion and Flame, Vol. 48, pp. 191–210, 1982.

27. Bradley, D., Hicks, M., Lawes, M., Sheppard, C. G. W. and Woolley, R., "The Measurement of Laminar Burning Velocities and Markstein Numbers for *iso*-Octane–Air and *iso*-Octane–*n*-Heptane–Air Mixtures at Elevated Temperatures and Pressures in an Explosion Bomb", Combustion and Flame, Vol. 115 pp. 126–144, 1998.
28. Liao, S. Y., Jiang, D. M., Huang, Z. H., Zeng, K. and Cheng, Q., "Determination of Laminar Burning Velocities for Mixtures of Ethanol and Air at Elevated Temperatures", Applied Thermal Engineering, Vol. 27, pp. 374–380, 2007.
29. Bradley, D., Lawes, M. and Mansour, M. S., "Explosion Bomb Measurements of Ethanol-Air Laminar Gaseous Flame Characteristics at Pressures up to 1.4 MPa", Combustion and Flame, Vol. 156, pp. 1462–1470, 2009.
30. Al-Shahrany, A. S., Bradley, D., Lawes, M. and Woolley, R., "Measurement of Unstable Burning Velocities of *iso*-Octane-Air Mixtures at High Pressure and the Derivation of Laminar Burning Velocities", Proceedings of the Combustion Institute, Vol. 30, pp. 225–232, 2005.
31. Jerzembeck, S., Peters, N., Pepiot-Desjardins, P. and Pitsch, H., "Laminar Burning Velocities at High Pressure for Primary Reference Fuels and Gasoline: Experimental and Numerical Investigation", Combustion and Flame, Vol. 156, pp. 292–301, 2009.
32. Gu, X., Huang, Z., Li, Q. and Chenglong, T., "Measurements of Laminar Burning Velocities and Markestein Lengths of *n*-Butanol-air Premixed Mixtures at Elevated Temperatures and Pressures", Energy and Fuels, Vol. 23, pp. 4900–4907, 2009.
33. Sarathy, S. M., Thomson, M. J., Togbe, C., Dagaut, P., Halter, F. and Mounaïm-Rousselle, C., "An Experimental and Kinetic Modeling Study of *n*-butanol Combustion", Combustion and Flame, Vol. 156, pp. 852–864, 2009.
34. Beeckmann, J., Kruse, S. and Peters, N., ''Effect of Ethanol and *n*-Butanol on Standard Gasoline Regarding Laminar Burning Velocities'', SAE Paper 2010-01-1452, 2010.
35. Beeckmann, J., Rohl, O. and Peters, N., ''Numerical and Experimental Investigation of Laminar Burning Velocities of *iso*-Octane, Ethanol and *n*-Butanol'', SAE Paper 2009-01-2784, 2009.
36. Beeckmann, J., Cai, L. and Pitsch, H., "Experimental Investigation of the Laminar Burning Velocities of Methanol, Ethanol, *n*-Propanol and *n*-Butanol at High Pressure", Fuel, Vol. 117, pp. 340–350, 2014.
37. Farrell, J. T., Johnston, R. J. and Androulakis, I. P., "Molecular Structure Effects on Laminar Burning Velocities at Elevated Temperature and Pressure", SAE Paper 2004-01-2936, 2004.
38. Marshall, S. P., Taylor, S., Stone, C. R., Davies, T. J. and Cracknell, R. F., "Laminar Burning Velocity Measurements of Liquid Fuels at Elevated Pressures and Temperatures with Combustion Residuals", Combustion and Flame, Vol. 158, pp. 1920–1932, 2011.
39. Vancoillie, J., Verhelst, S. and Demuynck, J., "Laminar Burning Velocity Correlations for Methanol-Air and Ethanol-Air Mixtures Valid at SI Engine Conditions", SAE Paper 2011-01-0846, 2011.
40. Broustail, G., Seers, P., Halter, F., Moreac, G. and Mounaïm-Rousselle, C., "Experimental Determination of Laminar Burning Velocity for Butanol and Ethanol *iso*-Octane Blends", Fuel, Vol. 90, pp. 1–6, 2011.

41. Broustail, G., Seers, P., Halter, F., Moreac, G. and Mounaïm-Rousselle, C., "Experimental Determination of Laminar Burning Velocity for Butanol/*iso*-Octane and Ethanol/*iso*-Octane Blends for Different Initial Pressures", Fuel, Vol. 106, pp. 310–317, 2013.
42. Bradley, D., Lawes, M. and Mansour, M.S., "The Problems of the Turbulent Burning Velocity", Flow, Turbulence and Combustion, Vol. 87, pp. 191–204, 2011.
43. Bradley, D., "Combustion and the Design of Future Engine Fuels", Proceedings of IMechE, Part C, Journal of Mechanical Engineering Science, Vol. 223, pp. 2751–2765, 2009.
44. Bradley, D., Lawes, M., Liu, K. and Mansour, M.S., "Measurements and Correlations of Turbulent Burning Velocities over Wide Ranges of Fuels and Elevated Pressures", Proceedings of the Combustion Institute, Vol. 34, pp. 1519–1526, 2013.
45. Lawes, M., Ormsby, M. P., Sheppard, C. G. W. and Woolley, R., "Variation of Turbulent Burning Rate of Methane, Methanol and *iso*-Octane Air Mixtures with Equivalence Ratio at Elevated Pressure", Combustion Science and Technology, Vol. 177, pp. 1273–1289, 2005.
46. Bradley, D., Lawes, M. and Mansour, M.S., "Correlation of Turbulent Burning Velocities of Ethanol-Air, Measured in a Fan-Stirred Bomb up to 1.2 MPa", Combustion and Flame, Vol. 158, pp. 123–138, 2011.
47. Serras-Pereira, J., Aleiferis, P. G., Richardson, D. and Wallace, S., "Mixture Formation and Combustion Variability in a Spray-Guided DISI Engine", Transactions of SAE, Journal of Engines, Vol. 116, No 3, pp. 1332–1356, Paper 2007-01-4033, 2007.
48. Serras-Pereira, J., Aleiferis, P. G., Richardson, D. and Wallace, S., "Characteristics of Ethanol, Butanol, *iso*-Octane and Gasoline Sprays and Combustion from a Multi-Hole Injector in a DISI Engine", SAE International Journal of Fuels and Lubricants, Vol. 1, pp. 893–909, SAE Paper 2008-01-1591, 2008.
49. Serras-Pereira, J., Aleiferis, P. G. and Richardson, D., "An Experimental Database on the Effects of Single and Split Injection Strategies on Spray Formation and Spark Discharge in an Optical DISI Engine Fuelled with Gasoline, *iso*-Octane and Alcohols. International Journal of Engine Research, 2014.
50. Serras-Pereira, J., Aleiferis, P. G. and Richardson, D., "An Analysis of the Combustion Behaviour of Ethanol, Butanol, *iso*-Octane, Gasoline and Methane in a Direct-Injection Spark-Ignition Research Engine. Combustion Science and Technology", Vol. 185, 484–513, 2013.
51. Aleiferis, P. G., Serras-Pereira, J. and Richardson, D., "Characterisation of Flame Development with Ethanol, Butanol, *iso*-Octane, Gasoline and Methane Fuels in a Direct-Injection Spark-Ignition Engine", Fuel, Vol. 109, 256–278, 2013.
52. Brequigny, P., Halter, F., Mounaïm-Rousselle, C., Moreau, B. and Dubois, T., "Thermodiffusive Effect on the Flame Development in Lean Burn Spark Ignition Engine", SAE Paper 2014-01-2630, 2014.
53. Mounaïm-Rousselle, C., Landry, L., Halter, F. and Foucher, F., "Experimental Characteristics of Turbulent Premixed Flame in a Boosted Spark-Ignition Engine", Proceedings of the Combustion Institute, Vol. 34, pp. 2941–2949, 2013.
54. Malcolm, J. S., Behringer, M. K., Aleiferis, P. G., Mitcalff, J. and OudeNijeweme, D., "Characterisation of Flow Structures in a Direct-Injection Spark-Ignition Engine using PIV, LDV and CFD", SAE Paper 2011-01-1290, 2011.

55. Aleiferis, P. G., Behringer, M. K., OudeNijeweme, D. and Freeland, P., "Integral Length Scales and Time Scales of Turbulence in an Optical Spark-Ignition Engine", Flow, Turbulence and Combustion, submitted, 2015.
56. Behringer, M. K., Aleiferis, P. G., OudeNijeweme, D. and Freeland, P., "Spray Formation from Spark-Eroded and Laser-Drilled Injectors for DISI Engines with Gasoline and Alcohol Fuels", SAE International Journal of Fuels and Lubricants, Vol. 7, pp. 803-822, Paper 2014-01-2745, 2014.
57. Behringer, M. K., Aleiferis, P. G., OudeNijeweme, D. and Freeland, P., "Spray Imaging and Droplet Sizing of Spark-Eroded and Laser-Drilled Injectors with Gasoline-Butanol and Gasoline-Ethanol Blends", Proceedings of International Conference on Fuel Systems for IC Engines, IMechE, London, pp. 179–198, 2015.
58. Ball, J. K., Raine, R. R. and Stone, C. R., "Combustion Analysis and Cycle-by-Cycle Variations in Spark Ignition Engine Combustion – Part 1: An Evaluation of Combustion Analysis Routines by Reference to Model Data", Proceedings of IMechE, Part D, Journal of Automobile Engineering, Vol. 212, pp. 381–399, 1998.
59. Stone, C. R. and Green-Armytage, D. I., "Comparison of Methods for the Calculation of Mass Fraction Burned from Engine Pressure-Time Diagrams", Proceedings of IMechE, Part D, Journal of Automobile Engineering, Vol. 201, pp. 61–67, 1987.
60. Brunt, M. F. and Emtage, A. L., "Evaluation of IMEP Routines and Analysis Errors", SAE Paper 960609, 1996.
61. Raffel, M., Willert, C. E., Wereley, S. T. and Komenhans, J., "Particle Image Velocimetry – A Practical Guide", 2nd Ed., Springer, 2007.
62. Behringer, M.K., "Effect of Ethanol and Butanol Content in Future Fuel Blends on Spray and Combustion Characteristics in DISI Engines", PhD Thesis, University College London, 2014.
63. Ihracska, B., Korakianitis, T., Ruiz, P., Emberson, D. R., Crookes, R. J., Diez, A. and Wen, D., "Assessment of Elliptic Flame Front Propagation Characteristics of *iso*-Octane, Gasoline, M85 and E85 in an Optical Engine", Combustion and Flame, Vol. 161, pp. 696–710, 2013.
64. Aleiferis, P. G., Taylor, A. M. K. P., Ishii, K. and Urata, Y., "The Nature of Early Flame Development in a Lean-Burn Stratified-Charge Spark-Ignition Engine", Combustion and Flame, Vol. 136, pp. 283–302, 2004.
65. Aleiferis, P. G. and Behringer, M. K., "Insights into Stoichiometric and Lean Combustion Phenomena of Gasoline–Butanol, Gasoline–Ethanol, *iso*-Octane–Butanol and *iso*-Octane–Ethanol Blends in an Optical SI Engine", Combustion Science and Technology, submitted, 2015.
66. Anbese, J. T., "Flame Development Study at Variable Swirl Level Flows in a Stratified CNG DI Combustion Engine using Image Processing Technique", Journal of Applied Sciences, Vol. 11, pp. 1698–1706, 2011.
67. Abdel-Gayed, R. G., Bradley, D. and Lawes, M., "Turbulent Burning Velocities: A General Correlation in Terms of Straining Rates", Proceedings of the Royal Society of London A, Vol. 414, pp. 389–413, 1987.

68. Bradley, D., "How Fast Can We Burn?", 24th Symposium (International) on Combustion, pp. 247–262, 1992.
69. Frazer, R. A. and Bracco, F. V., "Cycle-Resolved LDV Integral Length Scale Measurements in an IC Engine", SAE Paper 880381, 1988.
70. Peters, N., "The Turbulent Burning Velocity for Large-Scale and Small-Scale Turbulence", Journal of Fluid Mechanics, Vol. 384, pp. 107–132, 199.
71. Kang, K. Y. and Baek, J. H., "Turbulence Characteristics of Tumble Flow in a Four-Valve Engine", Experimental Thermal and Fluid Science, Vol. 18, pp. 231–243, 1998.
72. Fu, J., Deng, B., Wang, Y., Yang, J., Zhang, D., Xu, Z. and Liu, J., "Numerical Study and Correlation Development on Laminar Burning Velocities of *n*-Butanol, *iso*-Octane and their Blends: Focusing on Diluent and Blend Ratio Effects", Fuel, Vol. 124, pp. 102–113, 2014.
73. Abdel-Gayed, R. G., Bradley, D., Hamid, M. N. and Lawes, M., "Lewis Number Effects on Turbulent Burning Velocity", 20th Symposium (International) on Combustion, pp. 505–512, 1984.
74. Abdel-Gayed, R. G., Al-Khishali, K. J. and Bradley, D., "Turbulent Burning Velocities and Flame Straining in Explosions", Proceedings of the Royal Society of London A, Vol. 391, pp. 393–414, 1984.
75. Bradley, D., Haq, M. Z., Hicks, R. A., Kitagawa, T., Lawes, M., Sheppard, C. G. W. and Woolley, R., "Turbulent Burning Velocity, Burned Gas Distribution and Associated Flame Surface Definition", Combustion and Flame, Vol. 133, pp. 415–430, 2003.
76. Bradley, D., Lawes, M. and Sheppard, C. G. W., "Combustion and the Thermodynamic Performance of SI Engines", Proceedings of IMechE, Part C, Journal of Mechanical Engineering Science, Vol. 214, pp. 257–268, 2000.
77. Chen, R.-H., Mitchell, B. G. and Ronney, P. D., "Diffusive-Thermal Instability and Flame Extinction in Nonpremixed Combustion", 24th Symposium (International) on Combustion, pp. 213–221, 1992.
78. Lowry, W. B., Serinyel, Z., Krejci, M. C., Curran, H. J., Bourque, G. and Petersen, E. L., "Effect of Methano-Dimethyl-Ether Fuel Blends on Flame Stability, Laminar Flame Speed and Markstein Length", Proceedings of the Combustion Institute, Vol. 33, pp. 929–937, 2011.
79. Poling, B. E., Prausnitz, J. M. and O'Connell, J. P., "The Properties of Gases and Liquids", 5th Ed., McGraw Hill, 2001.
80. Yaws, C.L., "Yaws' Handbook of Thermodynamic and Physical Properties of Chemical Compounds", Knovel Electronic Database, 2003.
81. Hirschfelder, J. O., Curtiss, C. F. and Bird, R. B., "Molecular Theory of Gases and Liquids", 2nd Ed., John Wiley and Sons, 1954.
82. Tian, G., Daniel, R., Li, H., Xu, H., Shuai, S. and Richards, P., "Laminar Flame Characteristics of *iso*-Octane/n-Butanol Blend-Air Mixtures at Elevated Temperatures", Energy and Fuels, Vol. 27, pp. 2327–2335, 2013.
83. Gu, X., Huang, Z., Li, Q. and Tang, C., "Measurement of Laminar Burning Velocities and Markstein Lengths of n-Butanol-Air Premixed Mixtures at Elevated Temperatures and Pressures", Energy Fuels, Vol. 23, pp. 4900–4907, 2009.

84. Aleiferis, P. G. and Rosati, M. F., “Flame Chemiluminescence and OH LIF Measurements in a Hydrogen-Fuelled Spark-Ignition Engine”, International Journal of Hydrogen Energy, Vol. 37, pp. 1797–1812, 2013.
85. Aleiferis P. G. and Rosati M. F., “Controlled Autoignition of Hydrogen in a Direct Injection Optical Engine”, Combustion and Flame, Vol. 159, pp. 2500–2515, 2013.
86. Augoye, A. K. and Aleiferis, P. G., Characterisation of Flame Development with Hydrous and Anhydrous Ethanol Fuels in a Spark-Ignition Engine with Direct Injection and Port Injection Systems. SAE Paper 2014-01-2623, 2014.
87. Atzler, F., Lawes, M., Sulaiman, S. A. and Woolley, R., “Effects of Droplets on the Flame Speed of Laminar *iso*-Octane and Air Aerosols”, 10th International Congress on Liquid Atomization and Spray Systems, ICLASS, August 2006, Kyoto, Japan, Paper ICLASS06-258, 2006.
88. Lawes, M. and Saat, A., “Burning Rates of Turbulent *iso*-Octane Aerosol Mixtures in Spherical Flame Explosions”, Proceedings of the Combustion Institute, Vol. 33, pp. 2047–2054, 2011.

LIST OF ABBREVIATIONS

AFR	Air to Fuel Ratio
AIT	After Ignition Timing
ATDC	After intake Top Dead Centre
BTDC	Before compression Top Dead Centre
CA	Crank Angle
COV	Coefficient Of Variation (=Mean/RMS)
DISI	Direct Injection Spark Ignition
EGR	Exhaust Gas Recirculation
EVC	Exhaust Valve Closure
EVO	Exhaust Valve Open
IMEP	Indicated Mean Effective Pressure
IVC	Intake Valve Closure
IVO	Intake Valve Open
LDV	Laser Doppler Velocimetry
LIF	Laser Induced Fluorescence
MFB	Mass Fraction Burned
PFI	Port Fuel Injection
PIV	Particle Image Velocimetry
RMS	Root Mean Square
RPM	Revolutions Per Minute
SI	Spark Ignition
TKE	Turbulent Kinetic Energy

LIST OF TABLES

LIST OF FIGURES

Table 1. Basic Fuel Properties.

Fuel Property	Ethanol	*n*-Butanol	*iso*-Octane	Gasoline
Molar mass [g/mol]	46.07	74.12	114.3	100–105
Density 20 °C [g/cm^3]	0.79	0.81	0.69	0.72
Density 80 °C [g/cm^3]	0.73	0.76	0.64	0.66
Flash point [°C]	12	30	-12	-43
DVPE at 20 °C [kPa]	6.4	0.8	5.7	35
DVPE at 37.8 °C (~RVP) [kPa]	16.1	2.2	11.8	72.4
DVPE at 80 °C [kPa]	100	16.4	50	208
Bubble Point (0.5 bar) [°C]	62.6	108.8	80	29.8
Expl. limit (upper) [vol%]	15	11.3	6	7.6
Expl. limit (lower) [vol%]	3.5	1.4	1	1.4
Latent heat (at T_{boil} [kJ/kg])	855	584	272	364
Latent heat (25 °C) [kJ/kg]	874	669	300	380–500
Stoichiometric AFR	9.0	11.1	15.1	14.6
Heating value [MJ/kg], [MJ/l]	26.9, 21.3	33.9, 27.5	44.6, 30.8	42.7, 32
RON	129	96	100	95
H/C, O/C	3, 0.5	2.5, 0.25	2.25, 0	1.92, 0

Table 2. Laminar Burning Velocities.

Conditions			Laminar burning velocity [cm/s]			
T [K]	p [bar]	ϕ [−]	Ethanol	*n*-Butanol	*iso*-Octane	Gasoline
393	1	1.0	63	58	51	–
358–373	5	1.0	31.0	32.0	30.0	31.0
358–373	10	1.0	27.5	28.0	27.0	28
393	1	0.8	48	46	38	–
358–373	5	0.8	22.0	22.0	21.0	22.0
358–373	10	0.8	17.5	18.0	17.0	19

Table 3. Engine Specifications.

Engine Parameter	Value
Displacement [cm^3]	475
Compression Ratio	9.8:1
Connection Rod Length [mm]	165.2
Number of Valves	2 Inlet, 2 Outlet
Inlet Valve Opening (IVO), Closing (IVC)	349.5° CA, -124.5° ATDC Firing
Exhaust Valve Opening (EVO), Closing (EVC)	118° CA, -359° ATDC Firing

Table 4. PIV Measurement Settings.

Engine Speed [RPM]	1500
Intake Pressure [bar]	0.5
Fuel Pressure [bar], Temperature [°C]	80, 80
Start Of Injection (SOI) [°CA ATDC]	60
Measurement Timing [°CA BTDC]	26
Resolution [μm/Pixel]	Tumble: 18.4, Swirl: 34.6
Pulse Separation [μs]	Tumble: 5, Swirl: 10
Laser Wavelength [nm]	532
Camera Resolution [Pixels]	2048×2048
Lens	Nikon 60 mm
Lens Aperture [f/]	11
Interrogation Area [Pixels]	32×32, 50% Overlap
Grid Engine	Nyquist

Table 5. Averaged Integral Length Scales on Tumble and Swirl Planes.

	Air	Ethanol	*n*-Butanol	*iso*-Octane	Gasoline
L_{uv} [mm]	4.0	4.6	3.9	4.5	4.0
L_{vw} [mm]	5.5	5.7	4.9	5.5	5.5

Table 6. Combustion Parameters.

Combustion Parameters	Ethanol	*n*-Butanol	*iso*-Octane
Laminar Burning Velocity, u_l [m/s]	0.42	0.42	0.36
Laminar Flame Thickness, δ_l [mm]	0.0193	0.017	0.0185
Chemical Reaction time, τ_l [ms]	0.046	0.041	0.052
Kolmogorov Length Scale, η [mm]	0.027	0.026	0.027
Kolmogorov Time Scale, τ_η [ms]	0.106	0.105	0.106
Turbulent Reynolds Number, Re_L [-]	1197	1212	1189
Lewis Number (Rich), *Le* [-]	0.92	0.91	0.92
Lewis Number (Lean), *Le* [-]	1.50	2.12	2.79
Damköhler Number, *Da* [-]	79.7	90.0	71.1
Kalovitz Number, $Ka=\tau_l/\tau_\eta$ [-]	0.43	0.39	0.49
Karlovitz Stretch Factor, $K=0.25(u'/u_l)^2 Re_L^{-1/2}$ [-]	0.092	0.091	0.126

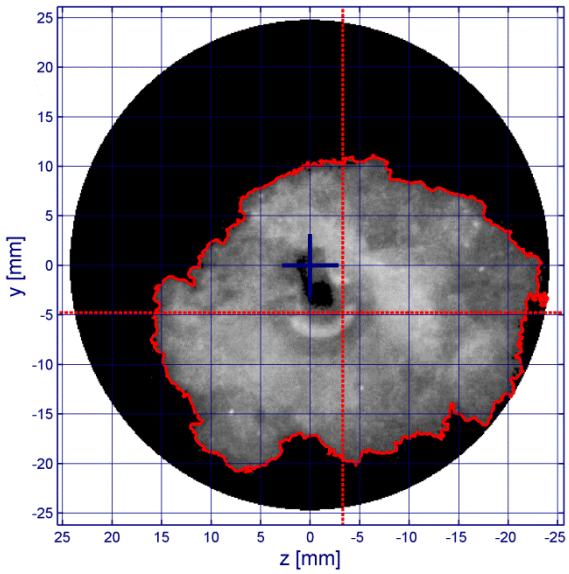

Figure 1. Typical flame chemiluminescence image; ethanol, 20 °CA AIT.

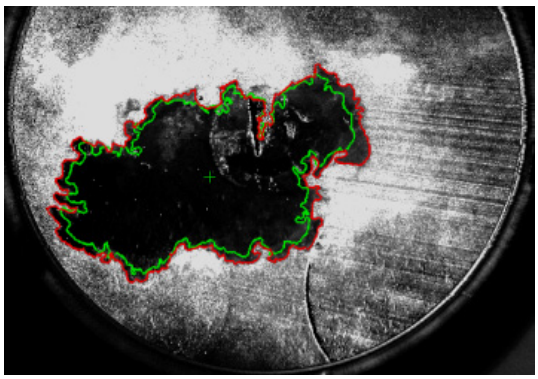

Figure 2. Typical double-pulsed flame tomography contours; gasoline, 15 °CA AIT. Frame A contour outlined in green and frame B contour outlined in red; 100 µs pulse separation.

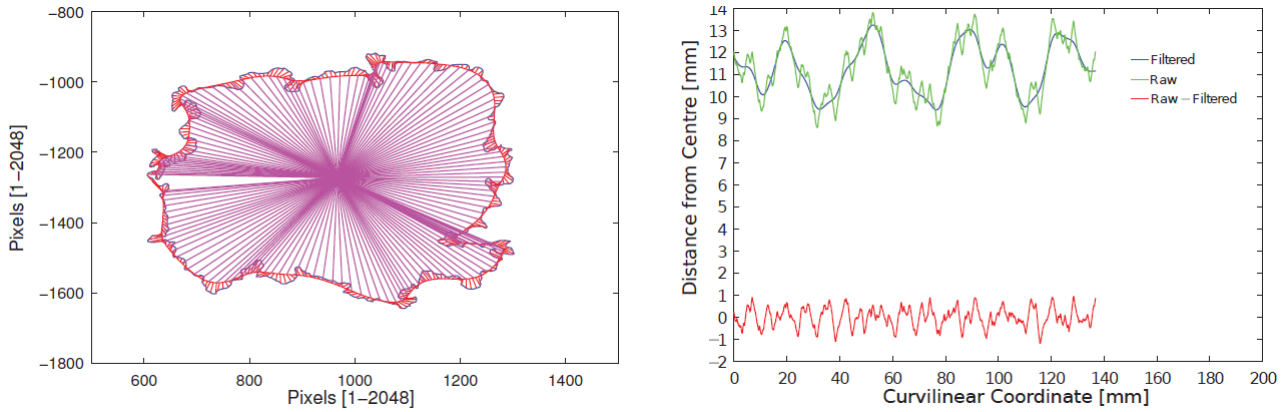

Figure 3. Flame tomography processing; left: raw (blue) and filtered flame (red) with distance to centre (magenta), right: raw (green) and filtered flame (blue) with their difference (red) *vs.* curvilinear coordinate.

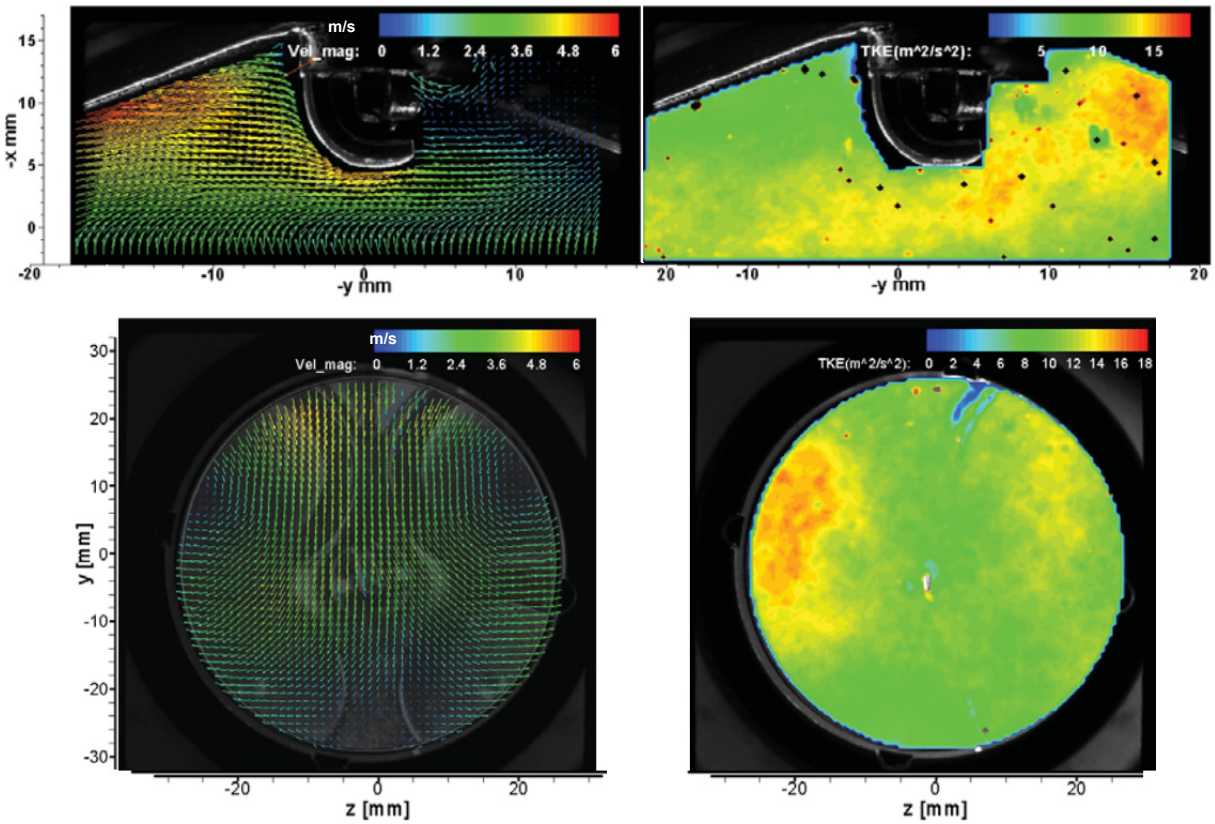

Figure 4. Mean flow and TKE, tumble plane (top), swirl plane (bottom); no fuelling (26 °CA BTDC).

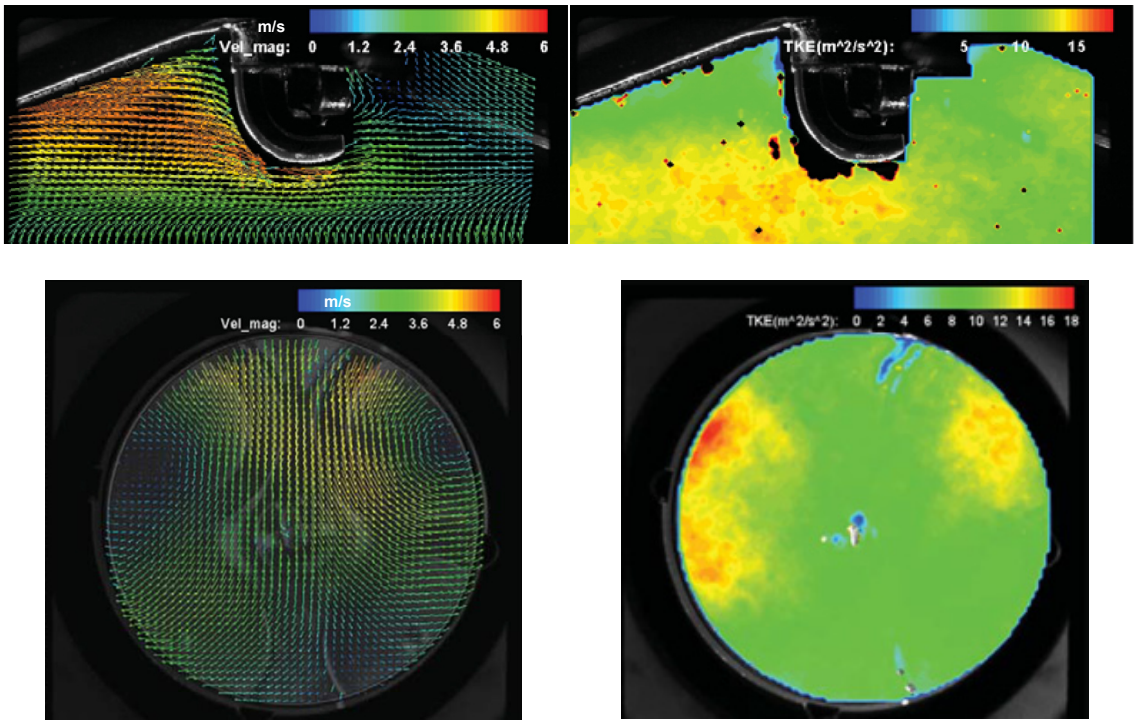

Figure 5. Mean flow and TKE, tumble plane (top), swirl plane (bottom); *iso*-octane fuelling (26 °CA BTDC).

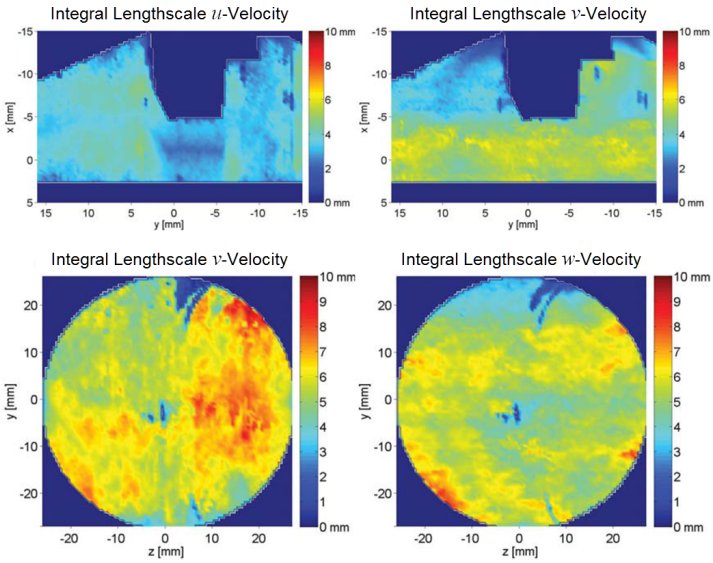

Figure 6. Tumble and swirl plane integral length scales, no fuelling (26 °CA BTDC).

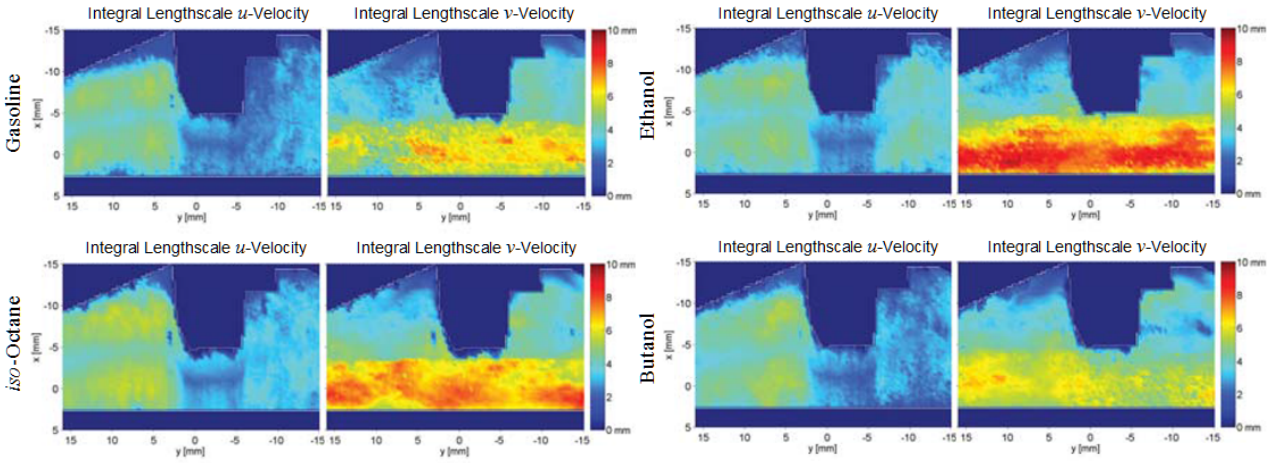

Figure 7. Tumble plane integral length scale maps with fuel injection (26 °CA BTDC).

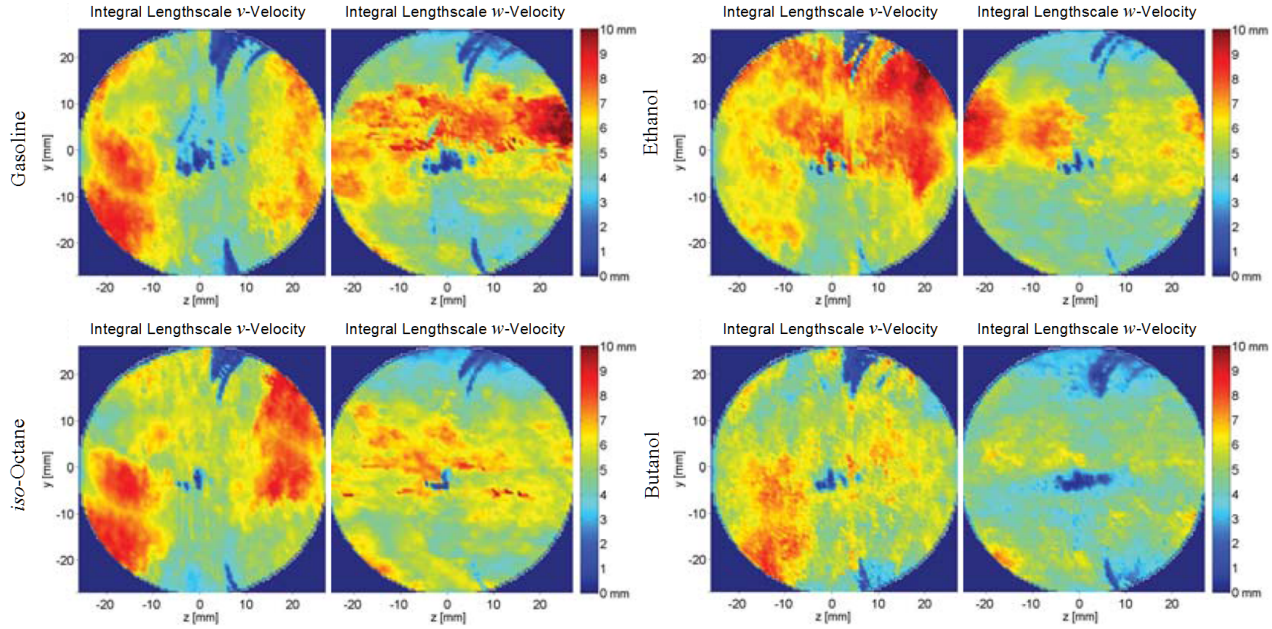

Figure 8. Swirl plane integral length scale maps with fuel injection (26 °CA BTDC).

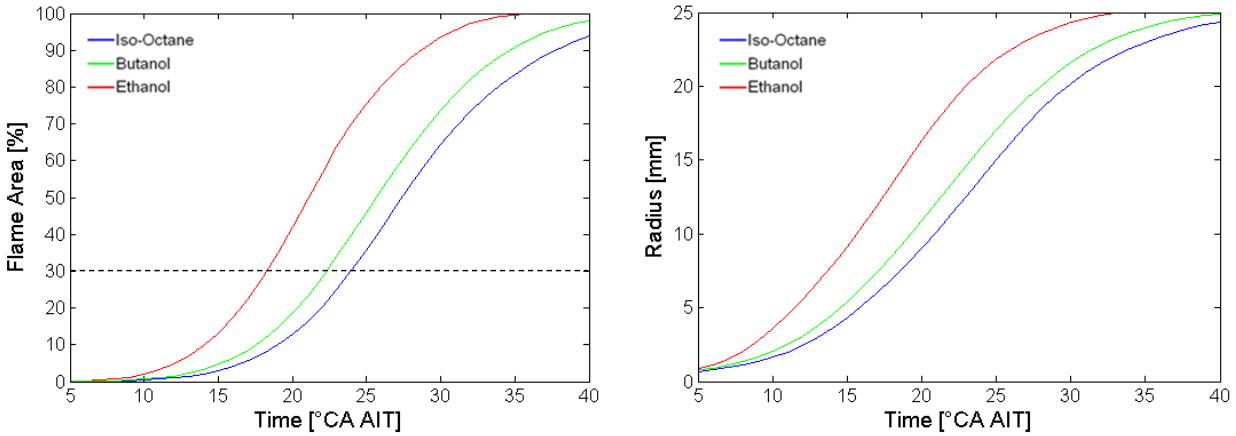

Figure 9. Growth of flame chemiluminescence area and radius during combustion.

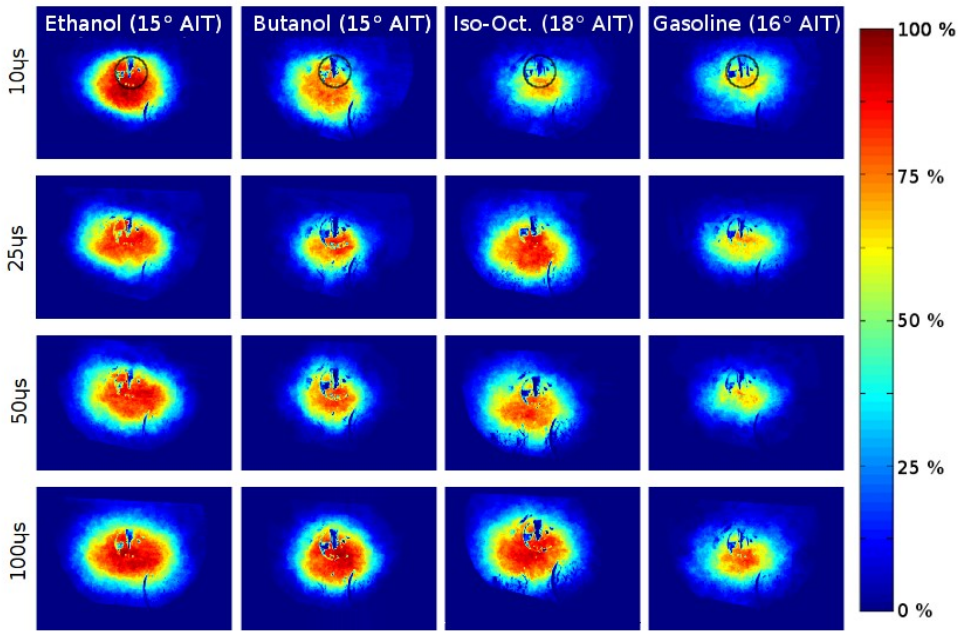

Figure 10. Probability of flame presence from tomography.

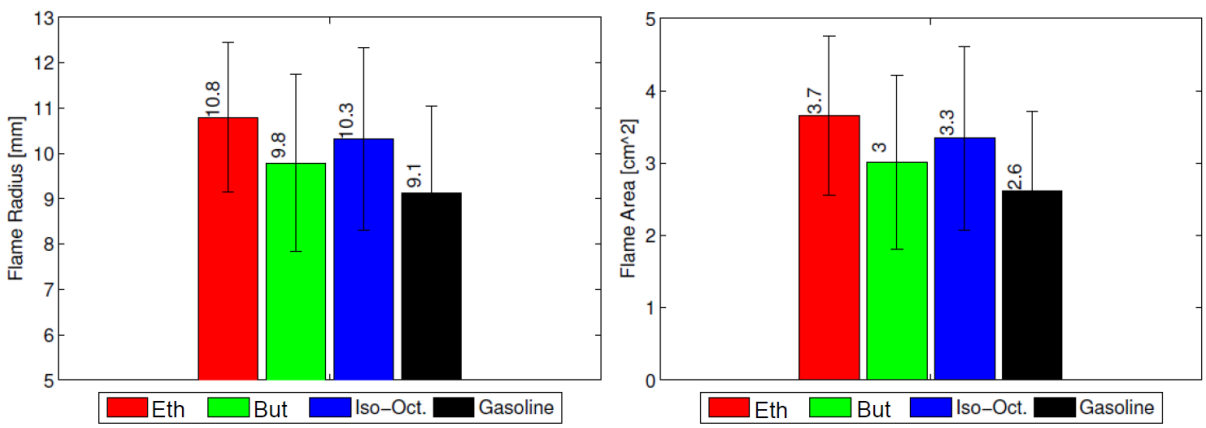

Figure 11. Flame radius and area from tomography.

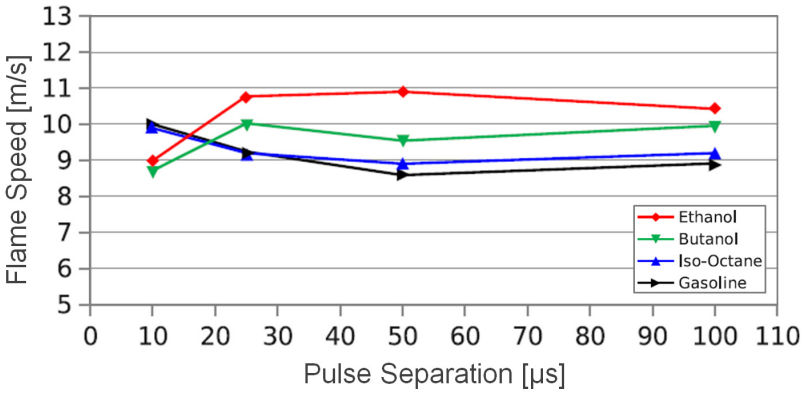

Figure 12. Equivalent flame radius growth rate *vs.* Laser pulse separation.

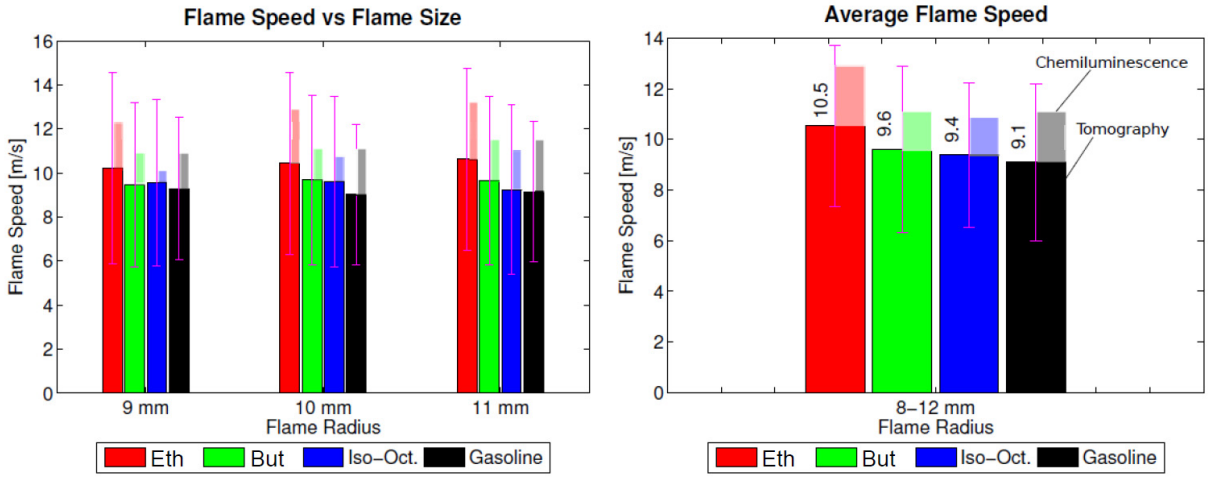

Figure 13. Flame radius growth rate from tomography for various flame sizes (left) and averaged over the region from 8–12 mm radius (right). Chemiluminescence equivalent results in light colouring.

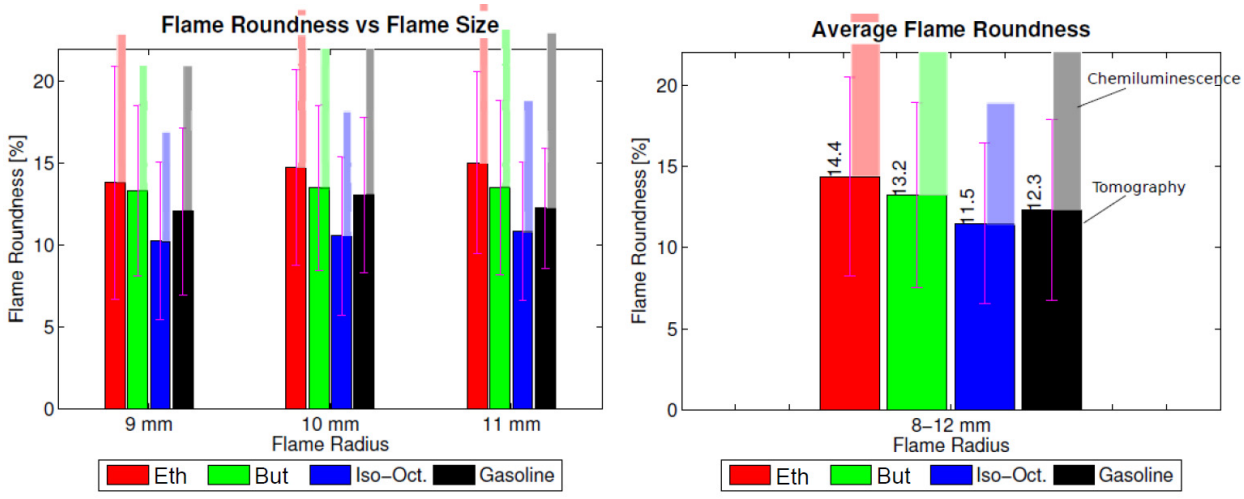

Figure 14. Flame roundness from tomography for various flame sizes (left) and averaged over the range 8–12 mm radius (right). Chemiluminescence equivalent results in light colouring.

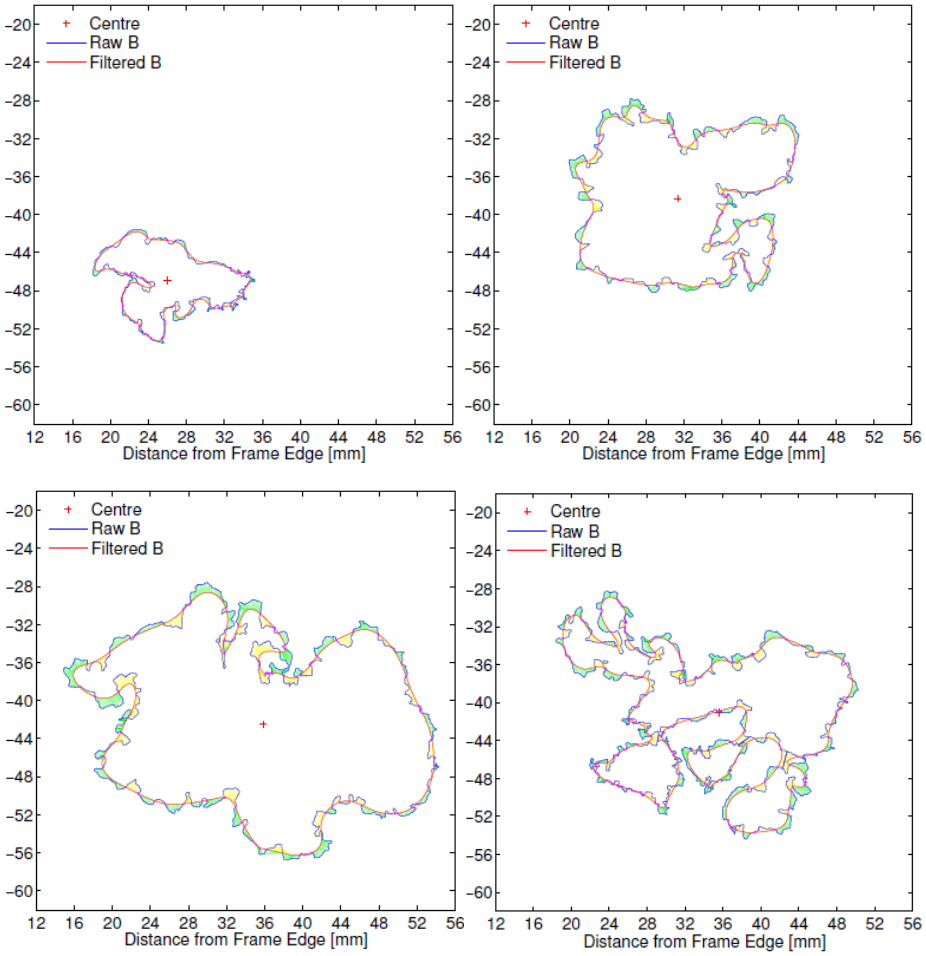

Figure 15. Outlining of flame front for small, medium, large and clustered flame sizes.

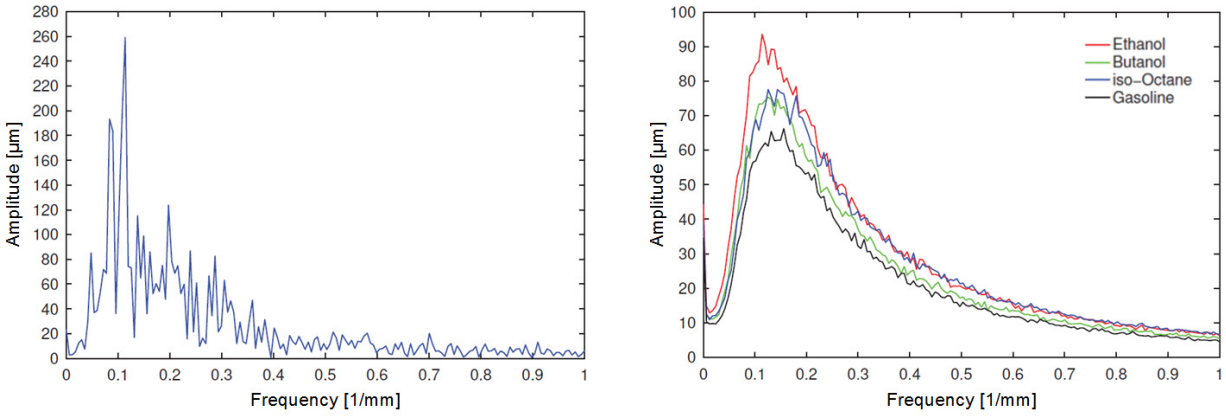

Figure 16. Fourier transform of the flame front fluctuation around the mean flame front for an individual image (left) and averaged over all images for each fuel (right).

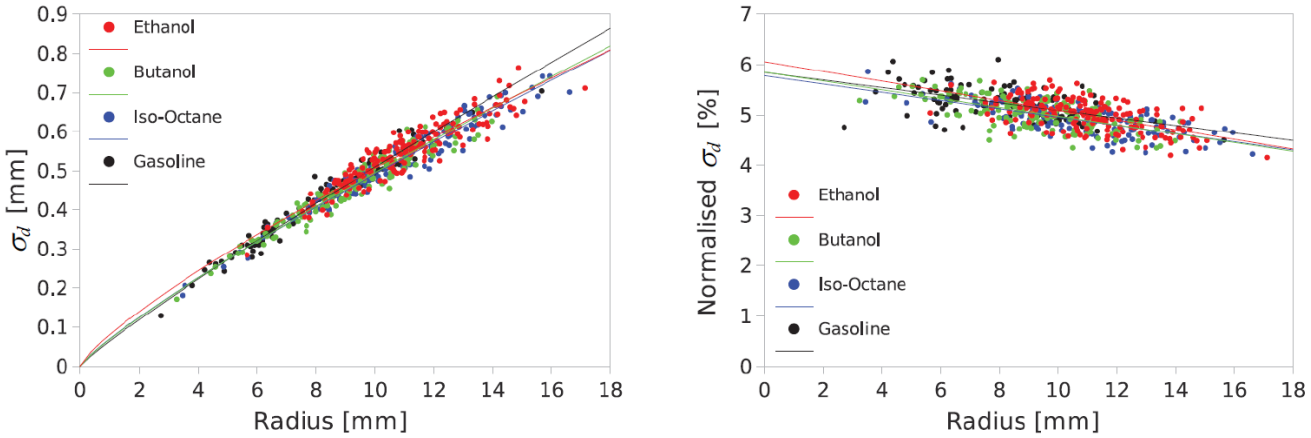

Figure 17. Standard deviation of displacement of instantaneous from filtered contour against flame radius; raw (left) and normalised by flame radius (right).

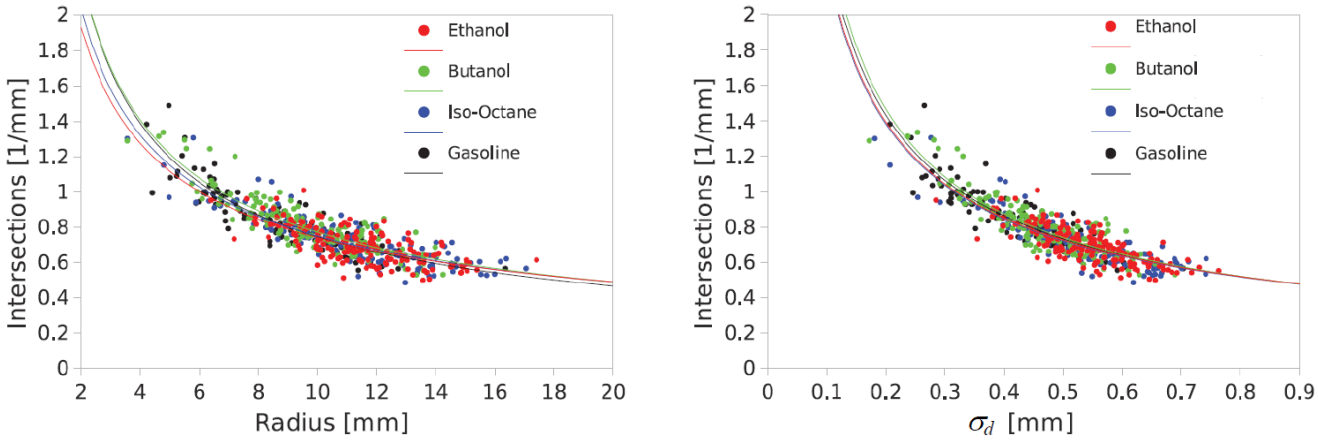

Figure 18. Flame front crossing point frequency against equivalent flame radius (left) and against standard deviation of displacement of instantaneous from filtered contour (right).

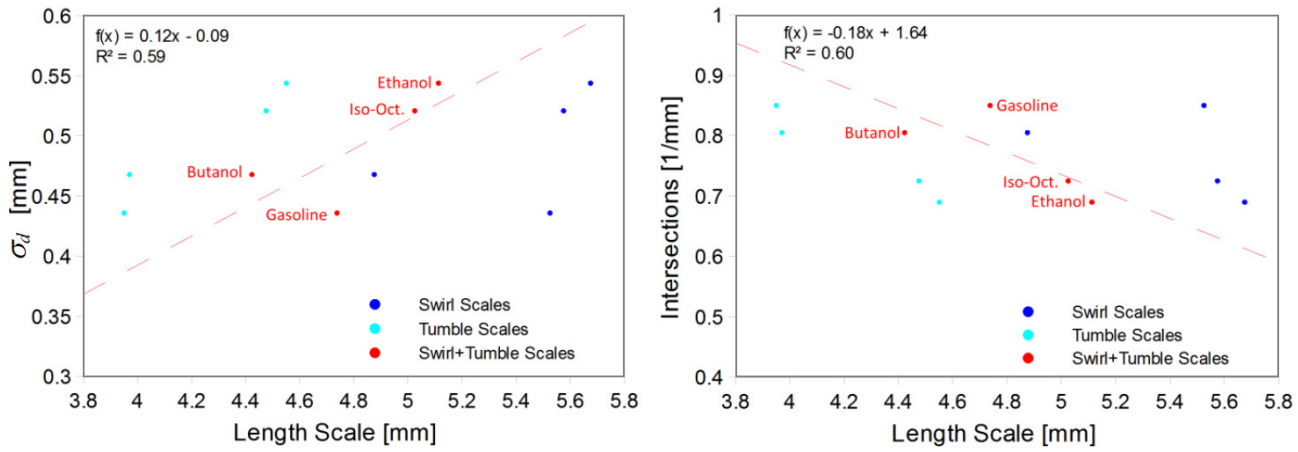

Figure 19. Crossing points and standard deviation of displacement of instantaneous from filtered contour against length scales.

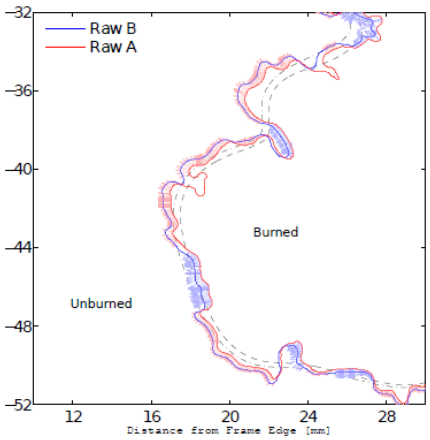

Figure 20. Localised flame crest and cusp velocities.

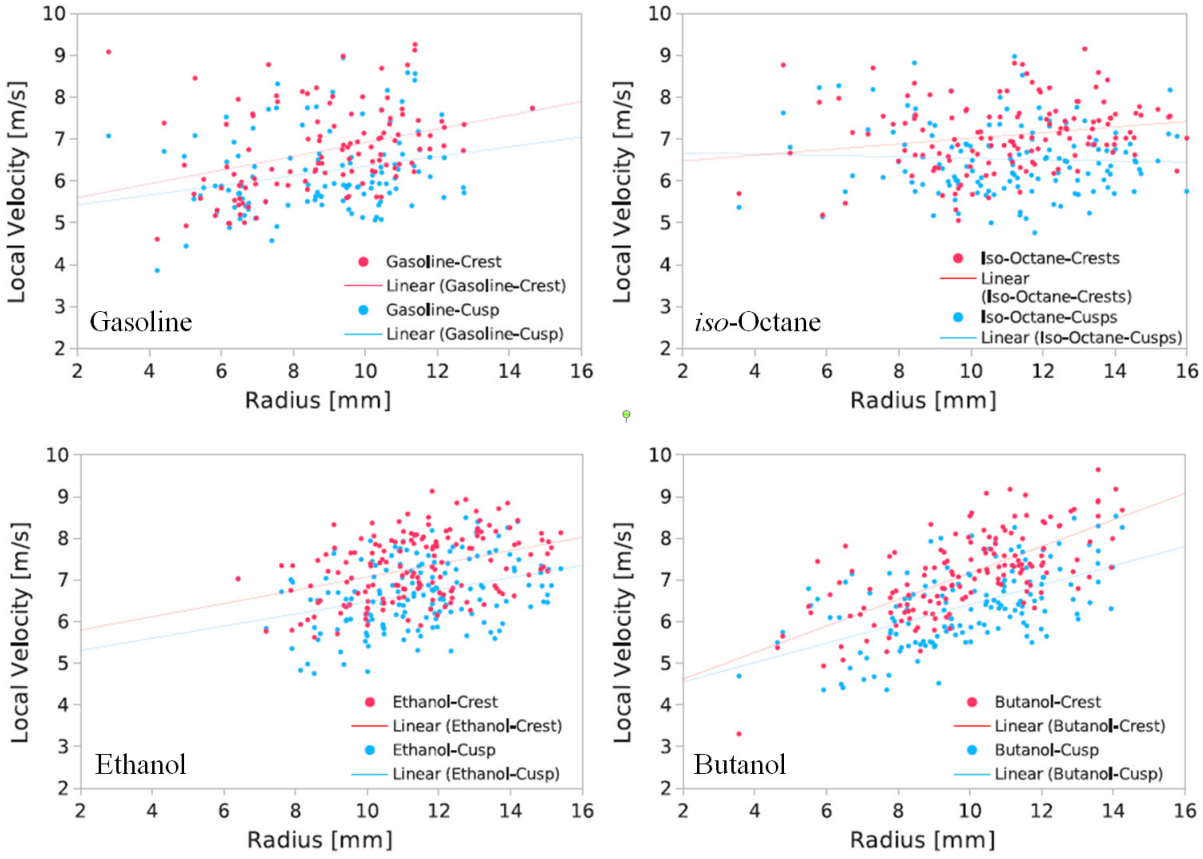

Figure 21. Localised flame crest and cusp velocities against flame radius.

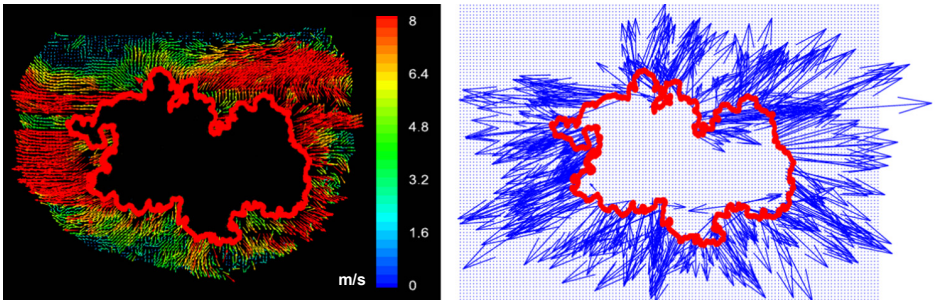

Figure 22. Flame contour and extraction of velocity vectors in the unburned gas and at the flame front.

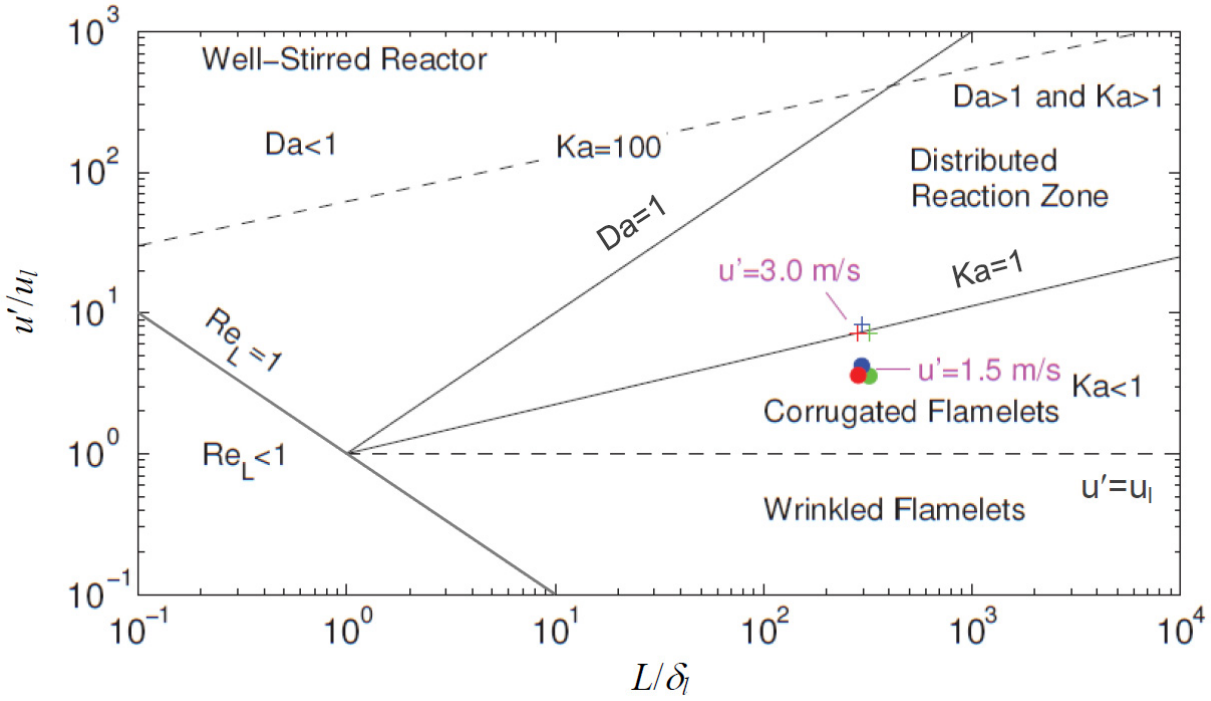

Figure A1. Combustion regime in the Peters-Borghi diagram (blue symbols: *iso*-octane, red symbols: ethanol, green symbols: butanol).